Table 2. Kinetic Parameters for the Decomposition of Substituted Benzisoxazoles

benzisoxazole	pK_a phenol	k_{AcO^-,H_2O} (M^{-1} s^{-1})	k_{AcO^-,CH_3CN} (M^{-1} s^{-1})	k_{BuNH_2,H_2O} (M^{-1} s^{-1})	k_{BuNH_2,CH_3CN} (M^{-1} s^{-1})	$(k_{cat}/K_m)_{34E4}$ (M^{-1} s^{-1})	$(k_{cat}/K_m)_{BSA}$ (M^{-1} s^{-1})
5,7-$(NO_2)_2$	0.6	2.76×10^{-3}	759 000			650 000	4530
5,6-$(NO_2)_2$	2.5	1.88×10^{-4}	57 800			3840	457
5-NO_2, 6-Cl	3.6	2.73×10^{-5}	4510	0.116	0.949	22 600	147
5-NO_2	4.1	1.33×10^{-5}	1000	0.0326	0.261	5450	23.9
5-CN	4.7	4.52×10^{-6}		0.0218	0.0603	144	1.81
6-NO_2	5.2	2.47×10^{-6}	104	0.0112	0.0247	0.177	1.52
5,6-Cl_2	5.6	1.52×10^{-6}		0.00854	0.0205	9.64	1.78
6-Cl	6.1		19.4			0.635	0.255
5-Cl	6.4					3.3	0.548
5-F	6.8		1.73			0.659	0.0218
unsubstituted	6.9		0.735			0.155	

[a] Experimental conditions: The second-order rate constants for the acetate and butylamine dependent reactions were determined in water or acetonitrile at 20 °C under pseudo-first order conditions as previously described. The reactions with 34E4 and BSA were performed in 40 mM phosphate, 100 mM NaCl, pH 7.4 and 20 °C.

Table 3. Relative Second Order Rate Constants and Brønsted Coefficients for the Decomposition of Substituted Benzisoxazoles

base/catalyst, medium	k_{rel}[a]	β_{lg}	r^2	no. of points
acetate, H_2O	1	-0.67 ± 0.01	0.998	8
acetate, CH_3CN	7.5×10^7	-0.95 ± 0.05	0.983	8
butylamine, H_2O	2.5×10^3	-0.53 ± 0.07	0.946	5
butylamine, CH_3CN	2.0×10^4	-0.86 ± 0.09	0.967	5
antibody 34E4, H_2O (pH 7.5)	4.1×10^8	-1.48 ± 0.13[b]	0.956	8
BSA, H_2O (pH 7.5)	1.8×10^6	-0.82 ± 0.07	0.946	10

[a] The second-order rate constant (k_{base} or k_{cat}/K_m) for the 5-NO_2 derivative. [b] Excluding 6-nitro, 5,6-dinitro, and 5,7-dinitrobenzisoxazoles, which deviate systematically from the correlation due to comparatively large K_m values (see Figure 2).

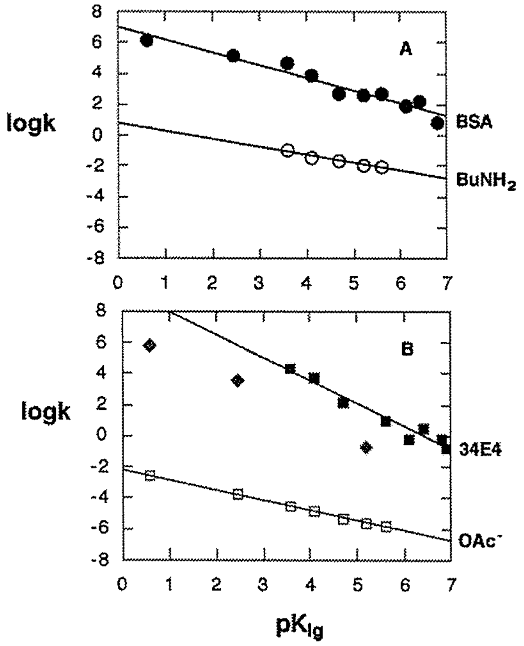

Figure 2. (A) Brønsted plot for the aqueous reaction of substituted benzisoxazoles with $BuNH_2$ (○) or with BSA (●). The apparent second-order rate constant $(k_{cat}/K_m)_{BSA}$ obtained at pH 7.4 was extrapolated to its maximum value using the known pH-dependence of the BSA-catalyzed reaction. (B) Brønsted plot for the aqueous reactions of BI with acetate (□) or 34E4 (■). The reactions of 34E4 with 5,7-dinitro-, 5,6-dinitro-, and 6-nitrobenzisoxazole (◆) deviate systematically from the correlation relating the other eight substrates.

along with the pK_a values of the leaving group of the corresponding phenols and the rate constants measured in water and acetonitrile (MeCN) with different bases and catalysts. Table 3 lists the β_{lg} values derived from the plots shown in Figure 2. Excellent LFERs are found for the eliminations promoted by butylamine or acetate as base, in both water and acetonitrile solvents, and with the catalytic antibody 34E4 and bovine serum albumin (BSA) as catalysts.

The β_{lg} values for these correlations vary from -0.53 to -1.48. In each case, the reaction rate increases with decreasing salicylonitrile pK_a, indicating substantial transfer of negative charge to the ether oxygen of the benzisoxazole in the transition state. The reactions involving acetate and butylamine in water have the smallest β_{lg} values; they are least sensitive to the stability of the leaving group. The similarity of the values suggests that the structures and strengths of the base have little influence on the transition state structure and its solvation in water. The change to acetonitrile as solvent causes a 10^8 acceleration with acetate as base, but only a 10-fold effect with the amine base. Despite dramatically different effects on the rates with different bases, the Brønsted β_{lg} values are -0.9 to -1.0 for both acetate and butylamine in acetonitrile. The values are close to -1, so that the effect of leaving group stability is strongly felt in the transition state. However, the aqueous pK_a values are used for this correlation, while one would expect a larger spread of pK_a values for a related nonpolar solvent. In the lower dielectric environment, there is greater sensitivity to charge development at oxygen.

These results can be compared and contrasted with those obtained with the protein catalysts BSA and antibody 34E4. BSA accepts a wide variety of mono- and di-substituted benzisoxazoles as substrates (Table 2), and the Brønsted β_{lg} value correlating these reaction rates is similar to that obtained with butylamine in acetonitrile. This suggests that the protein binding pocket that contains Lys222, the likely catalytic base,[9,17] presents a microenvironment to the developing phenoxide that is similar to that of acetonitrile.

Antibody 34E4 likewise accepts a wide range of substituted benzisoxazoles as substrates, but as shown in Figure 2, the reaction rate is unusually sensitive to leaving group effects. Eight of the eleven substrates tested are correlated with $\beta_{lg} = -1.5$, which is much larger than any of the other Brønsted coefficients. In this environment, the elimination rates respond more to substituent effects than aqueous pK values do. This mostly likely

---

(17) Carter, D. C.; Ho, J. X. *Adv. Prot. Chem.* **1994**, *45*, 153–203.

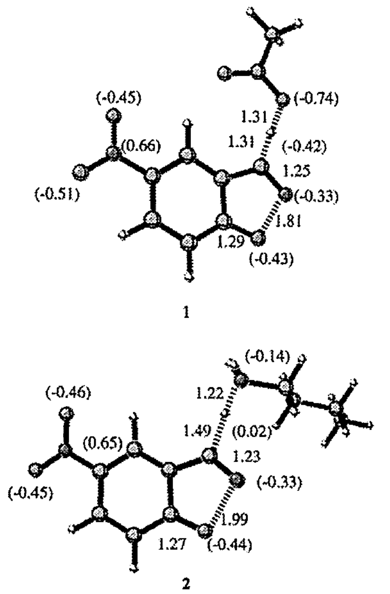

1

2

Figure 3. Computed transition states for reaction of acetate and butylamine with 4-nitrobenzisoxazole. Relevant bond lengths and charges are shown.

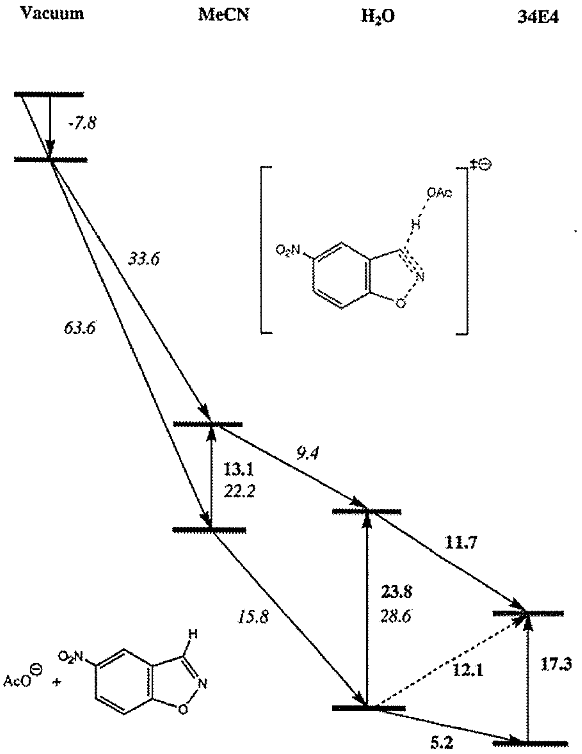

Figure 4. Free energy (ΔG) diagrams for reactions of acetate with 4-nitrobenzisoxazole in gas phase, acetonitrile, water, and antibody 34E4. Numbers in bold face are experimental values and those in italics are the averaged calculated values based on PCM and CPCM models.

arises from the enhanced basicity of the phenoxide leaving group in a relatively nonpolar environment, which leads to a larger spread in phenoxide pK values than in water or acetonitrile and a β value greater than -1.

The Brønsted plot for k_{cat} similarly yields $\beta_{lg} = -1.5$ ($r^2 = 0.97$) as a consequence of the similar K_m values (100–200 μM) exhibited by these substrates. Benzisoxazoles containing a nitro substituent at the 6- or 7-position deviate negatively from the correlation in 34E4 shown in Figure 2 and appear to lie along a line that is roughly parallel to that through the data for the other substrates. These substrates have substantially larger K_m values than the others, suggesting that they adopt a different binding mode at the active site. However, the large kinetic isotope effect ($V/K^D = 5.7$) measured for the most reactive compound, 5,7-dinitrobenzisoxazole ($k_{cat} = 660$ s^{-1}, $K_m = 1.0$ mM), shows that CH bond-breaking is still rate limiting for these substrates. The large β value for 34E4 indicates that the developing negative charge is relatively destabilized by the environment so that the substituent effects are very large, and reflect the very large role of substituent, rather than micro-environment, on charge stabilization. The results suggest that the local environment of 34E4 around the leaving group is effectively less polar than acetonitrile.

Quantum Mechanical Studies of the Base-Promoted Benzisoxazole Ring-Opening. Quantum mechanical calculations[18] and solvation energy estimations[19–22] were performed as described in the Experimental Section. The optimized geometries of the two transition states with acetate and butylamine as bases in the gas phase are shown in Figure 3. The proton is more completely transferred in the amine reaction, but the C—(H)—O and C—(H)—N distances are similar, at 2.62 and 2.71 Å, respectively. The lengths of the breaking N—O bonds in the five-membered ring are 1.81 and 1.99 Å in the two transition states, respectively. The charges on nitrogen (−0.33) and oxygen (−0.44) of the cleaving benzisoxazole ring are almost identical. Therefore, the E2 type geometry of the Kemp ring-opening does not change significantly with different bases.

The calculated activation barrier in the gas phase is −7.8 kcal/mol for the acetate catalyzed reaction, because there is an ion−molecule complex between the ionic reactant, acetate, and benzisoxazole, which is lower in energy than the reactants and the transition state for elimination. The conversion of this complex to the transition state has a normal positive activation barrier in solutions.

Solvation Energy Calculations. The calculated solvation free energies of acetate are all within 3 kcal/mol of the experimental aqueous solvation free energy of acetate (−77 kcal/mol).[23] The free energies of reactants and transition states in solvents are sums of the single point solvation free energies based on the

---

(18) Gaussian 98, Revision A.9, Frisch, M. J.; Trucks, G. W.; Schlegel, H. B.; Scuseria, G. E.; Robb, M. A.; Cheeseman, J. R.; Zakrzewski, V. G.; Montgomery, J. A.; Stratmann, Jr., R. E.; Burant, J. C.; Dapprich, S.; Millam, J. M.; Daniels, A. D.; Kudin, K. N.; Strain, M. C.; Farkas, O.; Tomasi, J.; Barone, V.; Cossi, M.; Cammi, R.; Mennucci, B.; Pomelli, C.; Adamo, C.; Clifford, S.; Ochterski, J.; Petersson, G. A.; Ayala, P. Y.; Cui, Q.; Morokuma, K.; Malick, D. K.; Rabuck, A. D.; Raghavachari, K.; Foresman, J. B.; Cioslowski, J.; Ortiz, J. V.; Baboul, A. G.; Stefanov, B. B.; Liu, G.; Liashenko, A.; Piskorz, P.; Komaromi, I.; Gomperts, R.; Martin, R. L.; Fox, D. J.; Keith, T.; Al-Laham, M. A.; Peng, C. Y.; Nanayakkara, A.; Challacombe, M.; Gill, P. M. W.; Johnson, B.; Chen, W.; Wong, M. W.; Andres, J. L.; Gonzalez, C.; Head-Gordon, M.; Replogle, E. S.; Pople, J. A. Gaussian, Inc., Pittsburgh, PA, 1998.

(19) Barone, V.; Cossi, M.; Tomasi, J. *J. Comput. Chem.* **1998**, *19*, 404–417.

(20) Miertus, S.; Scrocco, E.; Tomasi, J. *Chem. Phys.* **1981**, *55*, 117–129.

(21) JAGUAR (Schrödinger, Inc., Portland, OR) Version 4.0, 2000.

(22) "AMSOL 6.5", Hawkins, G. D.; Giesen, D. J.; Lynch, G. C.; Chambers, C. C.; Rossi, I.; Storer, J. W.; Rinaldi, D.; Liotard, D. A.; Cramer, C. J.; Truhlar, D. G.

(23) Pearson, R. G. *J. Am. Chem. Soc.* **1986**, *108*, 6109–6114.

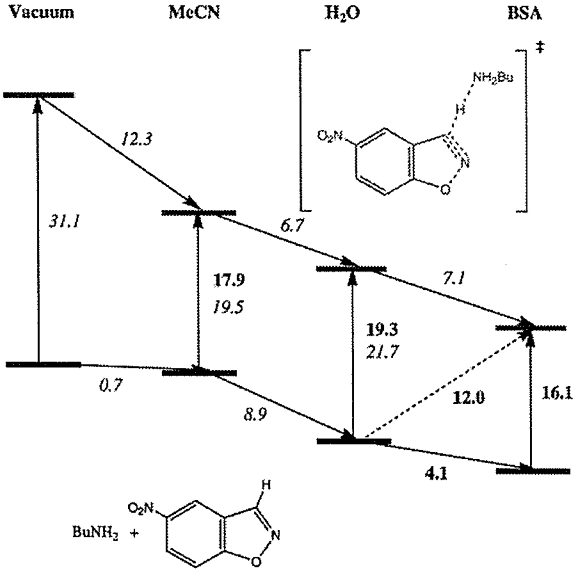

Figure 5. Free energy (ΔG) diagrams for reactions of butylamine with 4-nitrobenzisoxazole in the gas phase, acetonitrile, water and BSA. Numbers in bold face are experimental values and those in italics are the averaged calculated values based on PCM and CPCM models.

gas-phase geometries, and the relevant free energies in the gas phase. All of the methods overestimate the activation barriers in both water and MeCN. The CPCM model shows a change in the activation energy (7 kcal/mol) from water to acetonitrile which is closes to the experimental value (11 kcal/mol).

Figure 4 summarizes the energetics of acetate- and 34E4-promoted eliminations. CPCM calculations predict that acetate and benzisoxazole are stabilized by a total of 63.6 kcal/mol in acetonitrile, while the transition state **1** is solvated by only 33.6 kcal/mol. Because the reactants are stabilized much more than the transition state, the activation barrier changes from −7.8 kcal/mol in the gas phase to 22.2 kcal/mol in acetonitrile. The reactants and transition state are stabilized further by 15.8 and 9.4 kcal/mol, respectively, when changing the solvent from acetonitrile to water. The new activation barrier is calculated to be 28.6 kcal/mol, which is 6.4 kcal/mol higher than in acetonitrile, experiment shows an even larger activation barrier increase of 10.7 kcal/mol. Larger basis sets are likely to improve agreement with experiment. For the acetate-promoted process, the gas phase activation barrier (and consequently all the others) is decreased by 2 kcal/mol.

For the amine-catalyzed reaction, summarized in Figure 5, the activation barrier in the gas phase is 31.1 kcal/mol due to the difficulty of charge separation in the gas phase. The reactants are barely solvated by acetonitrile (0.7 kcal/mol), while the transition state is stabilized by 12.3 kcal/mol due to its high polarity. This leads to a smaller activation barrier (19.5 kcal/mol) in acetonitrile than in the gas phase. The additional changes of solvation free energies upon transfer from acetonitrile to water for reactants and transition state **2** are 8.9 and 6.7 kcal/mol, respectively. The resulting activation barrier in water (21.7 kcal/mol) is slightly higher than in acetonitrile, because the reactants are stabilized more than transition state. These calculations show good agreement with experiment for both acetonitrile and water.

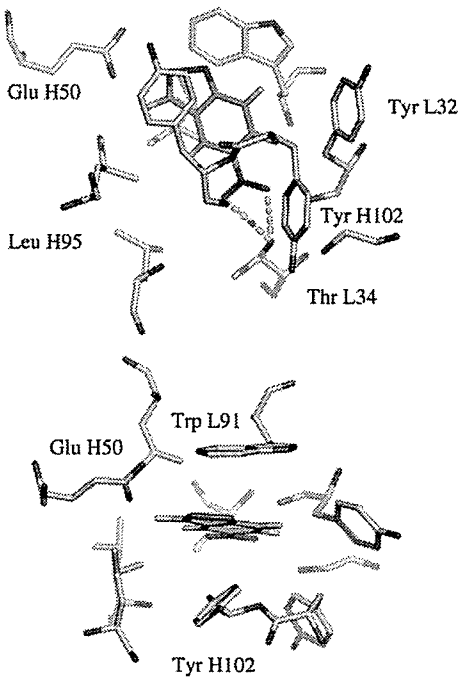

Figure 6. Docked binding mode of TS minus AcO^- in the 34E4 binding site. (a) Side view (b) Top view.

Acetate has an experimental pK_a value of 4.8 in water and 22.3 in acetonitrile,[24] and this large change is reflected in the large rate acceleration of the elimination in acetonitrile. However, experiment and calculation show that there is only a 2∼3 kcal/mol barrier change for the amine-catalyzed reaction. The small activation barrier change in the amine-catalyzed reaction is related to the smaller pK fluctuation from 10.8 in water to 18.3 in acetonitrile.[23]

Transfer of Substrates and Transition States from Water to Protein. The binding energies for reactants, estimated from measured K_m values, are 5.2 and 4.1 kcal/mol for 34E4 and BSA, respectively. The calculated free energy corresponding to k_{cat}/K_m is 12.1 kcal/mol for the reaction catalyzed by 34E4 and 12.0 kcal/mol for BSA. These results are also shown in Figures 4 and 5. According to the thermodynamic cycle, 34E4 and BSA stabilize the transition states by 11.7 and 7.1 kcal/mol relative to water, respectively. In acetate- and amine-catalyzed reactions, both the reactants and transition states are stabilized upon proceeding along the series from vacuum to acetonitrile, water, and protein. The protein catalysis occurs by lowering the free energy of the transition state in the protein complex more than the substrate in the protein complex. A similar trend was also found in our study of another solvent sensitive reaction, the antibody-catalyzed Kemp decarboxylation.[25]

Docking Studies with 34E4. To explore in detail the mechanism of antibody catalysis, the substrate and transition state were docked into the binding sites of 34E4. In the absence of a crystal structure for 34E4, we used a homology-based model

---

(24) Kolthoff, I. M.; Chantoon, M. K.; Bhowmik, S. *J. Am. Chem. Soc.* **1968**, *90*, 23–28.

(25) Ujaque, G.; Tantillo, D.; Hu, Y.; Houk, K.; Hotta, K.; Hilvert, D. *J. Comput. Chem.* **2003**, *24*, 98–110.

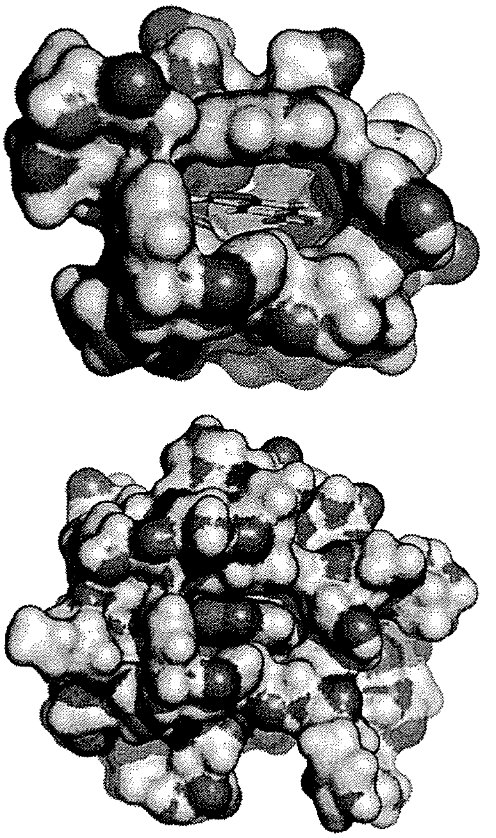

Figure 7. 34E4 surface including residues within 5 Å (top) and 8 Å (bottom) of the docked transition state.

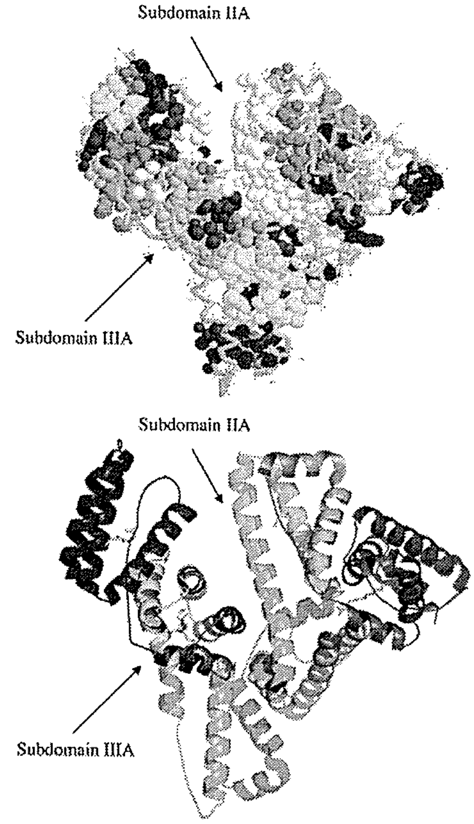

Figure 8. Human serum albumin. (a) Binding pockets and cavities calculated by CAST (b) The docked transition state and the myristic acid inhibitor.

based on the sequence of 34E4 obtained here (see Experimental Section). Figure 6 shows the best transition state docking mode for the acetate-catalyzed reaction in 34E4 in both side and top views. It has an estimated free energy of binding of −7 kcal/mol, according to the AUTODOCK free energy scoring function. In the vicinity of the benzisoxazole moiety, there are mostly hydrophobic residues. The nitro group is buried in the bottom of the 34E4 binding pocket, and forms two hydrogen bonds with Thr L34. The tight steric fit of the substrate within the pocket also suggests why substituents at the 6-position influence substrate binding (K_m) to a considerable extent in kinetic experiments (Table 2). Near the entrance to the binding site, the benzisoxazole transition moiety is surrounded by Tyr L32, Trp L91, Tyr H102, Tyr H103, and Glu H50, all of which are within 5 Å of the transition state. A potential base, Glu H50 is placed perfectly to deprotonate the benzisoxazole and initiate ring-opening. The distance of the nearest carboxylate oxygen from the transferring proton is 2.5 Å. The proposed role in catalysis is consistent with preliminary mutagenesis results showing that activity is abolished when GluH50 is substituted with glutamine.[27]

Figure 7 shows the solvent accessible surfaces of the 34E4 binding pocket including residues within 5 Å (top) or 8 Å (bottom) of the transition state. The transition state is trapped deeply inside the complementary binding pocket, which has a very narrow entrance formed by several hydrophobic residues. The second view shows that the transition state in 3D representation is in relatively tight contact with the surroundings. The region of negative electrostatic potential (red) is concentrated on the Glu H50 side, near where the proton of the benzisoxazole is located.

Antibody 34E4 provides a preorganized microenvironment made of hydrophobic and polar residues around the reaction center, with the basic site oriented for deprotonation of the benzisoxazole. The oxygen of the benzisoxazole ring is situated so as to be solvated by external water as it is transformed into cyanophenoxide.

Serum Albumin Catalysis. Serum albumins are ubiquitous proteins in the blood stream; albumins bind various small molecules in multiple binding sites. Hilvert and Kirby's experiment show that BSA and human serum albumin (HSA) have similar effects on the benzisoxazole elimination, and there is a binding site with lysine group present in each case.[5] Because the BSA crystal structure is unavailable, we used the HSA crystal structure for the docking study.

Two binding pockets with the highest CAST score (see Experimental Section) are the most likely binding sites (Figure 8). Subdomains IIA and IIIA, shown as light yellow and light blue, are also the two sites that have been proposed to bind small heterocyclic substrates such as warfarin experimen-

---

(26) Morris, G. M.; Goodsell, D. S.; Halliday, R. S.; Huey, R.; Hart, W. E.; Belew, R. K.; Olson, A. J. *J. Comput. Chem.* **1998**, *19*, 1639–1662.
(27) Seebeck, F., unpublished results.

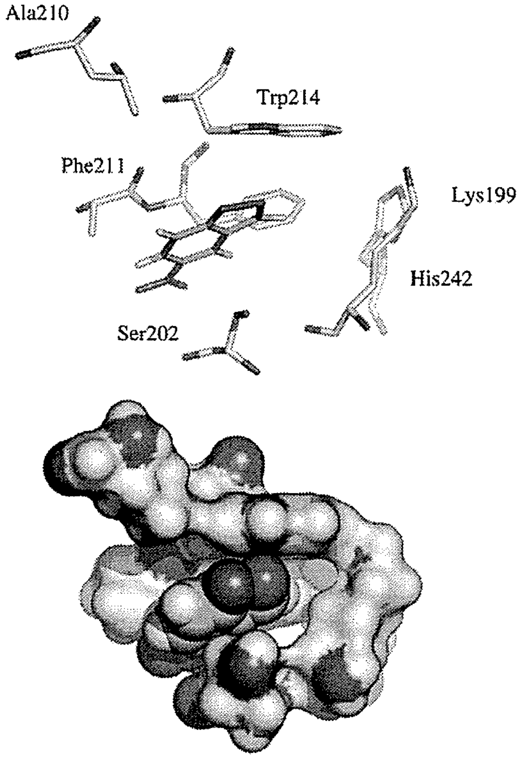

Figure 9. Transition state moiety in HSA subdomain IIA. (a) Residues within 5 Å of the transition state (b) Surface representation of residues within 5 Å of the transition state.

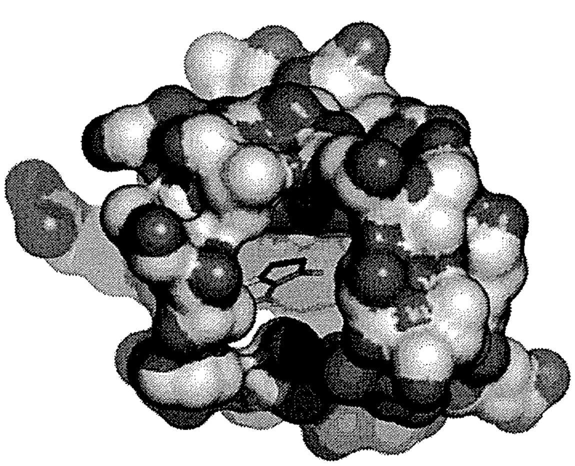

Figure 10. Surface representation of residues within 8 Å of the transition state.

tally.[29,30] The five myristic acids determined from the same crystal structure are shown in the second view (Figure 8b). Although there are lysine residues on the HSA surface, none of them can be considered as effective catalytic bases because of their high pK_a values on the protein surface. There is one lysine in subdomain IIA and no lysine residues inside the subdomain IIIA. Consequently, we focused our attention on the IIA subdomain.

Autodock produced a binding mode that is shown in Figures 9 and 10. The average estimated free energy of binding is -6 kcal/mol. Figure 9 shows stick and space-filling renderings of the protein with the transition state surrounded by residues in the cleft of subdomain IIA within 5 Å. The pocket has mainly nonpolar residues including Trp 214, Ala 219, Phe 211, Ser 202, His 242, and the putative base, Lys 199. The latter is 5.4 Å away from the transferring hydrogen. The only tryptophan in albumin, Trp214, has $\pi-\pi$ interactions with benzisoxazole aromatic ring. There is barely enough room for the transition state to stay in such a steep and narrow pocket. This can be seen from the comparison of 5 Å (Figure 9b) and 8 Å (Figure 10) surfaces. The transition state resides in the concave part of the binding pocket. Such a binding mode is not easily accessible from outside without conformational changes of the albumin upon binding the ligand. Lys 195 is located in subdomain IIA next to Lys 199. The protonation states of these two lysine groups have been studied both experimentally and theoretically. The combination of a neutral Lys 199 and protonated Lys 195 is the most favored one since they can form a hydrogen bond with water.[31] Experiments show that Lys 199 has a low pK_a (~8).[32] Therefore, we postulate that Lys 199 is the catalytic group in human serum albumin, whereas Lys222 is the catalytic group in bovine serum albumin. Experiments also indicate that HSA loses most of its catalytic ability upon Lys199 modification,[5] confirming the predictions from docking experiments.

Conclusion

The mechanisms of catalysis of the Kemp elimination have been elucidated for reactions occurring in two proteins, and the rates have been computed in aqueous and nonpolar solvents. Antibody 34E4 catalyzes this reaction by the alignment of catalytic base Glu H50 and substrate benzisoxazole within a relatively nonpolar pocket. Similarly, HSA has a deep nonpolar pocket at subdomain IIA with Lys 199 that can deprotonate 5-nitrobenzisoxazole.

An analogy between enzymes and organic solvents is often made, but the heterogeneous microenvironment of a protein pocket is clearly different from free solvent molecules in that its fixed structure can be tuned to interact with and stabilize disparate components of a reacting molecule. The efficiency of these biological catalysts derives from having a catalytic base geometrically positioned in a generally nonpolar active site, a consequence of successful hapten design in 34E4, but serendipitous in albumin. From the evolutionary perspective, there is no fundamental difference between our specific residue positioning argument and Kirby's more recent proposal of a specific medium effect.[9,33] The specific medium effect involves dispersion and electrostatic interactions with the transition state, which is a necessary outcome of the specific group positioning. The ultimate biological catalyst must utilize a perfect match

---

(28) (a) Liang, J.; Edelsbrunner, H.; Woodward, C. *Protein Science* **1998**, *7*, 1884–1897. (b) Liang, J.; Edelsbrunner, H.; Fu, P.; Sudhakar, P. V.; Subramaniam, S. *Proteins* **1998**, *33*, 1–17.

(29) Bhattacharya, A. A.; Grune, T.; Curry, S. *J. Mol. Biol.* **2000**, *303*, 721–732.

(30) Zaton, A. M. L.; Villamor, J. P. *Chem.-Biol. Interact* **2000**, *124*, 1–11.

(31) (a) Diaz, N.; Suarez, D.; Sordo, T. L.; Merz, Jr., K. M. *J. Med. Chem.* **2001**, *44*, 250–260. (b) Bhattacharya, A. A.; Petitpas, I.; Twine, S.; East, M.; Curry, S. *J. Biol. Chem.* **2001**, *276*, 22 804–809.

(32) (a) Gerig, J. T.; Reiheimer, J. D. *J. Am. Chem. Soc.* **1975**, *97*, 168–173. (b) Gerig, J. T.; Katz, K. E.; Reinheimer, J. D. *Biochim. Biophys. Acta* **1978**, *534*, 196–209.

(33) Hollfelder, F.; Kirby, A. J.; Tawfik, D. S. *J. Am. Chem. Soc.* **1997**, *119*, 9578–9579.

between the catalytic group and the transition state plus an elaborate active site made of polar and nonpolar groups, which provides favorable interactions with the transition state including electrostatics, solvation and other factors.[34] The most important feature for catalysis is the assembly of catalytic functionality, here the basic site, with appropriate orientation and reactivity. Of course catalysts that accidentally have an appropriate environment do exist, such as albumins in this case.

Catalytic antibodies represent a successful effort to biological catalyst design for nonbiological reactions. The problems in such design and execution are known[5] to be difficult but not insoluble.[36,37] A remaining challenge is how to use the programmable nature of the antibody pocket along with medium effects to act in concert with other active site parameters. Careful design by increasing the strength of the catalytic base through desolvation and by providing specific stabilizing interactions with the leaving group such as forming hydrogen bonds with phenoxide, should lead to better catalysts for such a solvent sensitive reaction.[38]

Experimental Section

Synthesis of Substituted Benzisoxazoles. Unsubstituted benzisoxazole and the 5-nitro-, 6-nitro-, 5,7-dinitro-, 5-chloro-, and 6-chloro-substituted derivatives were prepared according to the literature.[1a,39] 4-Cyano- and 4-fluorosalicylaldehyde were prepared from the corresponding phenols by a Duff reaction;[40] 4,5-dichlorosalicylaldehyde was prepared by a Reimer–Tiemann reaction.[41] The substituted salicylaldehydes were converted to benzisoxazoles by a standard literature procedure.[39b]

5-Cyanobenzisoxazole. ^{1}H NMR (300 MHz, $CDCl_3$) δ 7.76 (q, 1H), 7.84 (q, 1H), 8.16 (d, 1H), 8.83 (d, 1 H). MS FABM$^+$ 145 (M^++H^+). mp 245 °C (decomp.).

5,6-Dichlorobenzisoxazole. ^{1}H NMR (300 MHz, $CDCl_3$) δ 7.80 (d, 1H), 7.85 (s, 1H), 8.68 (d, 1H). MS FABM$^+$ 187/189 (M^++H^+), 210/212 (M^++Na^+). mp 92 °C (sub.).

5-Fluorobenzisoxazole. ^{1}H NMR (300 MHz, $CDCl_3$) δ 7.32 (q, 1H), 7.38 (q, 1H), 7.59 (q, 1H), 8.7 (d, 1 H). MS FABM$^+$ 139 (M^++H^+). mp 68 °C (sub.).

5,6-Dinitrobenzisoxazole. 6-Nitrobenzisoxazole (200 mg) was dissolved in ice-cooled cH_2SO_4 (1.6 mL). Fuming nitric acid (200 μl) was added dropwise, and the reaction mixture was heated at 80 °C for 30 min. The starting material was completely consumed. The reaction mixture was poured onto ice and then extracted immediately with methylene chloride. The organic layer was dried and purified by silica gel chromatography using methylenechloride as eluent to give 142 mg of the desired product in 56% yield. ^{1}H NMR (300 MHz, $CDCl_3$) δ 8.17 (q, 1H), 8.52 (d, 1H), 9.15 (d, 1H). MS FABM$^+$ 210 (M^++H^+). mp 112 °C.

5-Nitro-6-chlorobenzisoxazole. 6-Chlorobenzisoxazole was nitrated at the 5-position by the same method used to prepare 5,6-dinitrobenzisoxazole in 62% yield. ^{1}H NMR (300 MHz, $CDCl_3$) δ 7.88 (d, 1H), 8.36 (d, 1H), 8.86 (d, 1H). MS FABM$^+$ 198/200 (M^++H^+). mp 106 °C.

Kinetic Analyses. All kinetic experiments were performed at 20 °C. Fast reactions were measured by stopped flow techniques. The reactions were initiated by adding the benzisoxazole substrate to the reaction mixture and product formation was monitored spectrophotometrically at the following wavelengths: 5,7-dinitro (352 nm), 5,6-dinitro (380 nm), 5-nitro-6-chloro (380 nm), 5-nitro (380 nm), 5-cyano (324 nm), 6-nitro (404 nm), 5,6-dichloro (342 nm), 6-chloro (329 nm), 5-chloro (339 nm), 5-fluoro (338 nm), and unsubstituted (325 nm). Extinction coefficients were measured for each compound under the reaction conditions. The second-order rate constants for the acetate and butylamine-dependent reactions were determined in water or MeCN at 20 °C. Pseudo-first-order rate constants were plotted against acetate or butylamine concentration, and the slope of these plots gave the second-order rate constant for the base-catalyzed reaction. The reactions with 34E4 and BSA were performed in 40 mM phosphate, 100 mM NaCl, pH 7.4 and 20 °C. Initial velocities were calculated by standard linear-regression analysis using the initial linear portion of absorbance vs time plots and were corrected for background activity. The k_{cat} and K_m values were calculated by fitting the kinetic data to the Michaelis–Menten equation using the program KaleidaGraph. Two percent acetonitrile was used to dissolve the substrate for all reactions in aqueous medium. Crystallized BSA, treated to remove bound lipids, was purchased from Sigma and used without further purification; 34E4 was isolated and purified as previously described.

Cloning of the Antibody Genes. Poly (A)$^+$ mRNA was isolated from the hybridoma producing antibody 34E4.[2] A cDNA library was constructed with the Great Lengths cDNA synthesis kit (Clontech). The V_L and V_H genes were cloned using the polymerase chain reaction with the following primers: V_L sense, GTACATTT*GCTCTTC*GGTTCACAGGCTGTTGTGACTCAGGAA (the *Sac* I restriction site is in italics); V_L anti-sense, ATGAGTTTTTGTTCT*GCGGCCGC*CTTGGGCTGACCTAGGACAGT (*Not* I); V_H sense AGGTCCAGCTG*CTCGAG*TCTGG (*Xho* I); V_H anti-sense GTTCTG*ACTAGT*GGGCACTCTGGGCTC (*Spe* I). The amplified fragments were purified, cloned into appropriate sites in the vector p4xH-M13[42] and sequenced. The resulting expression plasmid, p4xH-34E4, allows production of 34E4 as a chimeric murine-human Fab fragment in which the V_L and V_H segments of the catalytic antibody are fused to human Cκ and gamma C_H1 regions, respectively.[42]

The antibody sequences for the variable segments of 34E4 are given in Chart 1.

Construction of a Homology Model. A search of the structure database identified antibodies HC19 (1gig.pdb)[43] and J539 (2fbj.pdb)[44] as having the highest sequence similarity to the 34E4 V_L and V_H domains, respectively. Because HC19 and 34E4 have CDR H3 loops that are the same length and that possess reasonable sequence similarity (28.6%), modeling of the V_L–V_H interface[45] is facilitated. A least-squares fit of the V_H domains of HC19 and J539, minus the CDR H3 loop, allowed overlay of the two molecules with a rmsd. of 1.40 Å for all Cα atoms except those of the CDR L1 (residues L24 to L34) and H3 (residues H95 to H102). In this overlay, the V_H domains of the two antibodies were superimposed with rmsd. of 0.88 Å for all non-CDR H3 Cα atoms, whereas the V_L domains were overlaid with rmsd. of 1.37 Å for all non-CDR L1 Cα atoms. In particular, the residues near the V_L/V_H interface from the two molecules, namely residues L42-L46, L94-L100, H43-H50, H58-H61, and H103-H105 (27 residues in total), coincided with each other with rmsd. of 0.87 Å for all Cα atoms. Accordingly, visual inspection of the interface between the HC19 V_L and J539 V_H domains revealed that no significant steric interference was introduced by the way the two domains were put together. After

---

(34) Houk, K. N.; Leach. A. G.; Kim, S. P.; Zhang, X. *Angew Chem., Int. Ed.* **2003**, *42*, 4872–4897.

(35) Zhang, X.; Houk, K. N., submitted for publication.

(36) Tantillo, D. J.; Houk, K. N. *J. Org. Chem.* **1999**, *64*, 3066–3076.

(37) Barbany, M.; Gutierrez-de-Teran, H.; Sanz, F.; Villa-Freixa, J.; Warshel, A. *ChemBioChem* **2003**, *4*, 277–285.

(38) Parker, A. J. *Chem. Rev.* **1969**, *69*, 1–32.

(39) (a) Kemp, D. S.; Woodward R. B. *Tetrahedron* **1965**, *21*, 3019–3035. (b) Casey, M. L.; Kemp, D. S.; Paul, K. G.; Cox, D. D. *J. Org. Chem.* **1973**, *38*, 2294–2301.

(40) Suzuki, Y.; Takahashi, H. *Chem. Pharm. Bull.* **1983**, *31*, 1751–1753.

(41) Postmus, C.; Kaye, I. A.; Craig, C. A.; Matthews, R. S. *J. Org. Chem.* **1964**, *29*, 2693–2698.

(42) Ulrich, H. D., Patten, P. A., Yang, P. L., Romesberg, F. E., & Schultz, P. G. *Proc. Natl. Acad. Sci. U.S.A.* **1995**, *92*, 11 907–11 911.

(43) Bizebard, T.; Daniels, R.; Kahn, R.; Golinellipimpaneau, B.; Skehel, J. J.; Knossow, M. *Acta Crystallog.* **1994**, *D50*, 768–777.

(44) Suh, S. W.; Bhat, T. N.; Navia, M. A.; Cohen, G. H.; Rao, D. N.; Rudikoff, S.; Davies, D. R. *Proteins: Struct. Funct. Genet.* **1986**, *1*, 74–80.

(45) Stanfield, R. L.; Takimoto-Kamimura, M., Rini, J. M.; Profy, A. T.; Wilson, I. A. *Structure* **1993**, *1*, 83–93.

Chart 1

34E4 light chain variable domain

1	2	3	4	5	6	7	8	9	10	11	12
gln	ala	val	val	thr	gln	glu	ser	ala	- - -	leu	thr
13	14	15	16	17	18	19	20	21	22	23	**24**
thr	ser	pro	gly	glu	thr	val	thr	leu	thr	cys	arg
25	**26**	**27**	**27A**	**27B**	**27C**	**28**	**29**	**30**	**31**	**32**	**33**
ser	ser	ser	gly	ala	val	thr	thr	ser	asn	tyr	ala
34	35	36	37	38	39	40	41	42	43	44	45
thr	trp	val	gln	glu	lys	pro	asp	his	leu	phe	thr
46	47	48	49	**50**	**51**	**52**	**53**	**54**	**55**	**56**	57
gly	leu	ile	gly	gly	thr	asn	lys	arg	ala	pro	gly
58	59	60	61	62	63	64	65	66	67	68	69
val	pro	ala	arg	phe	ser	gly	ser	leu	ile	gly	asp
70	71	72	73	74	75	76	77	78	79	80	81
arg	ala	ala	leu	thr	ile	thr	gly	ala	gln	thr	glu
82	83	84	85	86	87	88	**89**	**90**	**91**	**92**	**93**
asp	glu	ala	ile	tyr	phe	cys	ala	leu	trp	asn	ser
94	**95**	**96**	**97**	98	99	100	101	102	103	104	105
asn	his	leu	val	phe	gly	gly	gly	thr	lys	leu	thr
106	106A	107	108	109	110						
val	leu	gly	gln	pro	(lys)*						

34E4 heavy chain variable domain

1	2	3	4	5	6	7	8	9	10	11	12
(glu)	val*	(lys)*	leu	leu	glu	ser	gly	gly	gly	leu	ala
13	14	15	16	17	18	19	20	21	22	23	24
gln	pro	gly	gly	ser	leu	lys	leu	ser	cys	ala	ala
25	26	27	28	29	30	**31**	**32**	**33**	**34**	**35**	36
ser	gly	phe	asp	phe	arg	arg	tyr	trp	met	thr	trp
37	38	39	40	41	42	43	44	45	46	47	48
val	arg	gln	ala	pro	gly	lys	gly	leu	glu	trp	ile
49	**50**	**51**	**52**	**52A**	**53**	**54**	**55**	**56**	**57**	**58**	**59**
gly	glu	ile	asn	pro	asp	ser	arg	thr	ile	asn	tyr
60	**61**	**62**	**63**	**64**	**65**	66	67	68	69	70	71
met	pro	ser	leu	lys	asp	lys	phe	ile	ile	ser	arg
72	73	74	75	76	77	78	79	80	81	82	82A
asp	asn	ala	lys	asn	ser	leu	tyr	leu	gln	leu	ser
82B	82C	83	84	85	86	87	88	89	90	91	92
arg	leu	arg	ser	glu	asp	ser	ala	leu	tyr	tyr	cys
93	94	**95**	**96**	**97**	**98**	**99**	**100**	**100A**	**B**	**C**	**D**
val	arg	leu	asp	phe	asp	val	tyr	asn	his	tyr	tyr
E	**F**	**101**	**102**	103	104	105	106	107	108	109	110
val	leu	asp	tyr	trp	gly	gln	gly	thr	ser	val	thr
111	112	113									
val	ser	ser									

Table 4. Comparison of Experimental and Calculated Solvation Free Energies and Nitrobenzisoxazole Elimination Activation Energies for Acetate-Catalysis with Different Theoretical Models

	solvation free energy in H_2O (kcal/mol)				solvation free energy in CH_3CN (kcal/mol)			
	AcO^-	NBI	TS	$\Delta\Delta G^\ddagger$	AcO^-	NBI	TS	$\Delta\Delta G^\ddagger$
CPCM[a]	−74.1	−5.2	−43.0	28.6	−63.0	−0.6	−33.6	22.2
PCM[a]	−75.3	−6.7	−43.5	30.7	−63.4	−0.6	−33.6	22.6
PB[b]	−77.4	−5.7	−46.4	28.9	−75.1	−12.4	−54.4	25.3
SM5.2R[c]	−77.3	−11.4	−51.6	29.3	−75.6	−15.7	−56.3	27.2
experiment	−77.0[d]			23.8	−62.7[e]			13.1

[a] B3LYP/6-31+G* with CPCM or PCM solvation models in Gaussian 98. [b] B3LYP/6-31+G* with Poisson−Boltzmann solvation model in Jaguar 4.0.[21] [c] AM1 with SM5.2R solvation model in AMSOL 6.5.[22] [d] Ref 23. [e] Pliego, Jr., J. R.; Riveros, J. M. *Phys. Chem. Chem. Phys.* **2002**, *4*, 1622.

the superimposition of the HC19 V_L and J539 V_H domains, residues H90 to H104 (the CDR H3-containing loop) of the J539 V_H domain were replaced by the corresponding loop residues from HC19 to form a HC19 V_L-J539 V_H chimera with the H3 loop from HC19. All residues were then manually modified, or mutated, to reflect the 34E4 sequence. For the "mutated" residues, the side-chain rotamer that gave the best fit to the local environment as judged by visual inspection was chosen. Other known structures were also consulted in remodeling the local sequence environment around the mutated residues when the change required a significant structural alteration. For example, replacing Met^{H82} with a branched leucine in the J539 V_H domain caused a steric clash with the surrounding residues. However, structural information from antibody CHA255 (1ind.pdb),[46] which has a leucine residue at position H82, helped resolve the problem.

Quantum Mechanical Methods. Both transition state geometries were optimized in the gas phase with Density Functional Theory (DFT)[47] at B3LYP/6-31+G(d) level with GAUSSIAN 98.[18] CHELPG[48] charges were obtained at B3LYP/6-31+G(d) level. Several solvation models including CPCM,[19] a polarizable conductor-like solvation model, PCM,[20] a polarizable continuum model, a Poisson−Boltzmann (PB) model[21] and the Cramer−Truhlar SM5.2R solvation model[22] were compared for solvation calculations on acetate-catalyzed reaction (Table 4). All solvation energies from continuum models (PCM and CPCM) are single point energies computed based on the geometries in the gas phase.

Docking Calculations. Autodock 3.0[26] was employed for docking purposes. Autodock uses a hybrid Lamarckian genetic algorithm (LGA) for docking and predicts the best binding modes according to an empirical scoring function that predicts the binding energy. Acetate was left out purposely from the gas-phase transition state docking experiments, since a carboxylate of an aspartate or glutamate in the binding site is considered to be the base. CHELPG charges were taken from the computed transition state structure in the gas phase. The receptor is fixed in all the dockings and represented by grid maps. The transition states do not have any torsional degrees of freedoms because of their structural rigidity. A total of 100 ga-run were conducted in each case and resulting conformations were clustered with 1 Å root-mean-square deviations (RMSD). The representative docked conformation of the best cluster in terms of binding free energy and population was chosen as the final binding mode.

Location of Binding Sites in HSA. The CASTp program was used to locate possible binding cavities and pockets for albumin using a solvent probe (sphere of 1.4 Å) analytically.[28] Multiple binding pockets and cavities for HSA (PDB ID: 1BJ5) have been found as shown in Figure 8 (top). This crystal structure includes five bound myristic acids. These were removed for the CASTp analysis. The spheres represent the surfaces of the key C, N, and O atoms that define the boundary between bulk solvent and protein pockets or cavities.

Acknowledgment. We thank Jim Na (Pfizer, La Jolla), Jeehiun K. Lee (Rutgers), and Qiaolin Deng (Merck) for preliminary results and extensive discussions. We are grateful to the National Institute of General Medical Sciences, National Institutes of Health (D.H. and K.N.H.) and National Science Foundation (K.N.H.) for financial support of this research and to the Naito Foundation (Tokyo, Japan) for a postdoctoral fellowship to K.K. We owe special thanks to UCLA Academic Technology Services (Y.H. and K.N.H.) and ETH and Novartis (D.H.).

JA0490727

---

(46) Love, R. A.; Villafranca, J. E.; Aust, R. M.; Nakamura, K. K.; Jue, R. A.; Major, Jr., J. G.; Radhakrishnan, R.; Butler, W. F. *Biochemistry* **1993**, *32*, 10 950−10 959.

(47) (a) Becke, A. D. *J. Chem. Phys.* **1993**, *98*, 5648−5652. (b) Lee, C. T.; Yang, W. T.; Parr, R. G. *Phys. Rev. B* **1988**, *37*, 785−789.

(48) (a) Chirlian, L. E.; Francl, M. M. *J. Comput. Chem.* **1987**, *8*, 894−905. (b) Breneman, C. M.; Wiberg, K. B. *J. Comput. Chem.* **1990**, *11*, 361−373.

JOURNAL OF CHEMICAL PHYSICS VOLUME 121, NUMBER 21 1 DECEMBER 2004

Experimental evidence of distance-dependent diffusion coefficients of a globular protein observed in polymer aqueous solution forming a network structure on nanometer scale

Akiko Masuda and Kiminori Ushida[a]
Riken (The Institute of Physical and Chemical Research), 2-1 Hirosawa, Wako, Saitama 351-0198, Japan

Goro Nishimura, Masataka Kinjo, and Mamoru Tamura
Research Institute for Electronic Science, Hokkaido University, Sapporo 060-0812, Japan

Hiroyuki Koshino, Koichi Yamashita, and Thomas Kluge[b]
Riken (The Institute of Physical and Chemical Research), 2-1 Hirosawa, Wako, Saitama 351-0198, Japan

(Received 14 June 2004; accepted 3 September 2004)

The distance dependence of the diffusion coefficient (DDDC) of a globular protein (cytchrome c) in aqueous hyaluronan (HA) solution, which is a model system for extracellular matrices (ECMs), was measured by a combination of three kinds of spectroscopic measurements of diffusion coefficients, the time and space samplings of which are different. The results of the three methods are plotted against the diffusion distance derived from the consideration of each experimental condition. Due to the characteristic morphology of HA with an effective mesh structure, the proteins showed two extreme diffusion modes: (1) short (<10 nm) diffusion with rare contact with polymer chains; (2) long (>100 nm) diffusion significantly disrupted by polymer chains showing an $\approx 30\%$ reduction in diffusion coefficient. The transition from the short diffusion to the long one occurs in a very narrow range (10–100 nm) of diffusion distance and this unique character of HA realizing anomalous diffusion should provide suitable environments for various bioactivities when involved in ECM. © *2004 American Institute of Physics.* [DOI: 10.1063/1.1810476]

I. INTRODUCTION

In recent years, several experimental techniques which enable the direct determination by a spectroscopic measurement of diffusion coefficients have become popular and they are frequently referred to as "diffusiometry" techniques, for example, by researchers engaged in NMR spectroscopy. Generally in inhomogeneous media, observable diffusion coefficients D_{obs} are not a constant because the mean square displacement of diffusing particles ($\langle r^2 \rangle$) does not increase linearly with time over a wide range, for example, nanoseconds to seconds.[1–4] In such situations, D_{obs} values should be different for individual experiments depending on its observation period τ_{obs}. In this paper, this dependence of D_{obs} on τ_{obs} is referred to as *the time correlation* of diffusion coefficients. On the other hand, D_{obs} is also expected to exhibit *the space correlation* depending on the scale of the sampling space for the observation.

Material transports showing spatiotemporal correlation are frequently referred to as "anomalous diffusion"[3–6] which was initially defined by Aharony and his co-workers.[5] This term is now widely used by theoretical physicists treating the diffusion in inhomogeneous media such as percolation clusters. It indicates the material transports of which mean-square displacement does not increase linearly on the time evolution,[3] i.e., $a \neq 1$ for $\langle r^2 \rangle \sim t^a$. Anomalous diffusion should play a crucial role particularly in various transports occurring in biological systems,[7–9] in functional matrices such as polymer gel solutions,[10–12] and colloid solutions.[13,14] For example, if a signaling molecule, such as a growth factor protein, is secreted at a certain position in organisms, it diffuses through extracellular or intracellular spaces until it reacts at the destination, such as an acceptor protein. In this sequence of secretion-diffusion-reaction, the transport (diffusion) period in the middle will govern a large part of the efficiency of the total bioactivity and the anomalous diffusion must be counted in almost all cases found in biological systems.[9] Moreover, the anomalous gradation of concentration would be formed in inhomogeneous media such as membranes, cytoplasm, and extracellular matrices (ECMs), to control the spatial yields of the biological reactions occurring in each organelle.[15–18]

Hyaluronan (HA),[19–24] a nonsulfated glycosaminoglycan of high molecular mass, is one of the most prominent members (saccharides and proteins) found in the ECM[25] of vertebrates. The most important role of HA is that of providing optimized environments for various bioactivities, the detailed mechanisms of which are still unclear. Even at a very low concentration (<1 wt%), HA forms effective network structures uniformly spread out in an aqueous solution,[22,25] the mesh size of which was previously estimated to be ≈ 10 nm at 1.5 wt% of HA by FRAP (Ref. 26) and electron spin resonance (ESR).[27] Therefore HA solution, which is a typical inhomogeneous medium, seems to be involved in many aspects of biological regulation through the transport

---

[a] Electronic mail: kushida@riken.jp

[b] Present address: Lohmann GmbH & Co. KG, Irlicher Str. 55, D-56567 Neuwied, Germany

0021-9606/2004/121(21)/10787/7/$22.00

of "particles" ranging from subnanometers (small molecules, ions) to micrometers (virus, cells) in diameter. The D_{obs} of the particles depends on the sizes of the particles relative to the mesh of HA and on diffusion time due to the retardation of diffusion by the network structure.

We have been focusing on the transport phenomena occurring in aqueous HA solutions[28–30] and have recently shown the experimental results of two methods in HA solutions using the same set of probe molecules for photochemical bimolecular reaction (PCBR) and pulsed field gradient (PFG) NMR.[30] Since these two methods have different τ_{obs} values that differ by $\approx 10^5$ times, i.e., 300–400 ns in PCBR and 10–100 ms in PFG-NMR, diffusing molecules travel extremely short distances ($L \sim 20$ nm) in PCBR or extremely long distances in PFG-NMR ($L \sim 10\ \mu$m). The D_{obs} obtained by PFG-NMR was $\approx 30\%$ smaller than that obtained by PCBR in 1.5 wt % HA solution: the obtained D_{obs} depended on τ_{obs}.

In the present paper, we report on our recent progress involving new results from the third experimental technique, fluorescence correlation spectroscopy (FCS),[31] to fill another region around $L \sim 200$ nm using cytochrome c (cytc) as a probe. A rough profile of the L (distance) dependence of the diffusion coefficient (DDDC) was obtained in the case of cytc in HA aqueous solution. DDDC proves the existence of two diffusion modes in sharp contrast which are mutually converted within a small region of $L = 10$–100 nm.

II. EXPERIMENTAL SECTION

A. Materials and fluorescence labeling

Horse heart cytochrome c Type VI (cytc; Sigma), tris(2,2′-bipyridine) ruthenium(II) complex [$\mathrm{Ru}(bpy)_3^{2+}$; Aldrich], methyl viologen (MV^{2+}; Nacalai), hexacyanoiron(III) complex [$\mathrm{Fe(CN)}_6^{3-}$; Wako], and tris(acetylacetonato) cobalt(III) [$\mathrm{Co}(acac)_3$; Dojindo], Alexa Fluor 488 (Alexa, Molecular Probes Inc.) were purchased and used without further purification. Ethylenediaminetetraacetate cobalt(III) [$\mathrm{Co}(edta)^-$] were prepared as described in the literature and purified by recrystallization. Alexa-labeled cytochrome c (Alexa-cytc) was synthesized using the succinimidyl ester of Alexa Fluor 488 carboxylic acid (Molecular Probes Inc.). Alexa-cytc was purified using a gel column and was dialyzed to remove unincorporated dye molecules. HA sample labeled molecular weight 300 000, of which real values in polydispersity was described elsewhere,[28] was obtained from Denki Kagaku Co., Ltd.

HA was dissolved in a buffer solution ($p\mathrm{H}=7$, ionic strength $= 0.1M$). The preparations of the aqueous HA solutions of the solutes mentioned above were described in our previous paper.[28–30]

B. Measurements

Since NMR and PCBR measurements were described in our previous paper in detail,[30] we only indicate the details of the FCS experiment here. The experimental setup for FCS (ConfoCor, Carl Zeiss Jena GmbH) consisted of an inverted microscope with an objective lens (*C*-Apochromat 40 ×/1.2), a cw Ar^+ laser (LGK 7812 ML, Carl Zeiss Jena GmbH), an avalanche photodiode (SPCM-200-PQ, EG&G) in the single-photon counting mode and a digital correlator (ALV 5000/E, ALV GmbH). A pinhole (30 μm in diameter) was set at the confocal image plane to eliminate the scattered light and emitted light coming from any place out of the focal plane.

A sample droplet of 200 μl was placed on a cover glass and covered with a small chamber to prevent evaporation during measurement. In order to determine focused volume (volume element), the diffusion coefficient of rhodamine $6G$ ($2.8 \times 10^{-6}\ \mathrm{cm^2\,s^{-1}}$) was used as a standard for calibration. The laser beam was focused on a very small optically well-defined open volume element where the fluorescent particles moved in and out by Brownian motion. The fluctuation of fluorescence intensity was analyzed by the normalized autocorrelation function $G(\tau)$:[31]

$$G(\tau) = \langle I(t) I(t+\tau)\rangle / \langle I\rangle^2 = 1 + \frac{\langle \delta I(t)\, \delta I(t+\tau)\rangle}{\langle I\rangle^2}. \tag{1}$$

Here, $I(t)$ is the detected fluorescence intensity and $\delta I(t)$ denotes the fluctuations of $I(t)$ around its mean $\langle I\rangle$. The brackets indicate time average. If fluorescence fluctuations arise only from the translational diffusion of the fluorescent molecules and the photochemical contribution of the dye molecules, the correlation function takes the form

$$G(\tau) = 1 + \frac{1}{N}\left\{\left[1+\frac{\tau}{\tau_D}\right]^{-1}\left[1+\frac{\tau}{q^2\tau_D}\right]^{-0.5} + f\exp\left(-\frac{\tau}{\tau_T}\right)\right\}, \tag{2}$$

where q is a structure parameter and is defined as $q = z/w$ (z and w are the axial and radial radii of the volume element, respectively), fraction f is the contribution of triplet-singlet conversion with a time constant τ_T, and N is the number density. By analyzing the observed correlation function using Eq. (2), the translational diffusion time τ_D of the molecules in the volume element was obtained. The diffusion coefficient D was determined using,

$$D = w^2/4\tau_D, \tag{3}$$

which is derived from the definition of τ_D. The laser power was adjusted by a set of ND filter to the intensity that brings the counting rate of 10–20 kcounts $\mathrm{s^{-1}}$ for the fluorescence intensity of Alexa in its ≈ 2 nM solution.

III. RESULTS AND DISCUSSION

A. HA concentration dependence of diffusion coefficients in the measurements of FCS and PFG-NMR

The diffusion coefficients D_{obs} of cytc labeled with a fluorescence probe (Alexa 488) and of only Alexa were measured by FCS at various concentrations of HA (C_{HA}) as shown in Fig. 1(a), normalized by the homogeneous diffusion coefficient D_0 that is obtained in the absence of HA. Curves a and b indicate cytc and Alexa, respectively. The raw experimental data of correlation functions for cytc are shown in Fig. 2. The fitting with Eq. (2) was successful

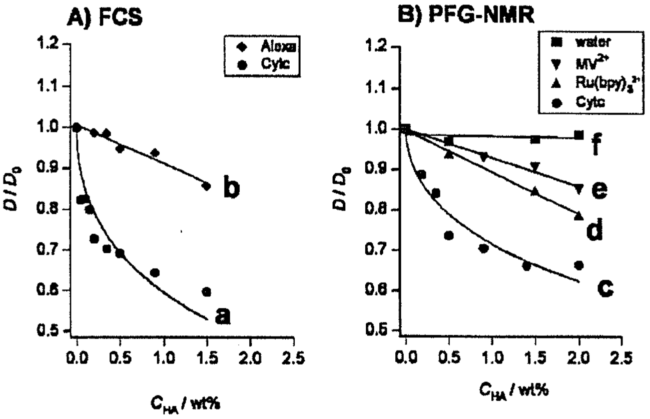

FIG. 1. Observed diffusion coefficients D_{obs} of cytc in aqueous HA solution at various concentrations, which is normalized to a relative value divided by nonperturbed diffusion coefficient D_0 at $C_{\mathrm{HA}}=0$: (A) Results from FCS for (a) Alexa-488-labeled cytc and (b) only Alexa. (B) Results of PFG-NMR (Ref. 30) for (c) cytc, (d) $\mathrm{Ru}(bpy)_3^{2+}$, (e) methylviologen (MV^{2+}), and (f) water. The fitting curves of cytc are obtained from Eq. (4) using $a=0.165$ and $a=0.105$ for a (FCS) and c (PFG-NMR), respectively.

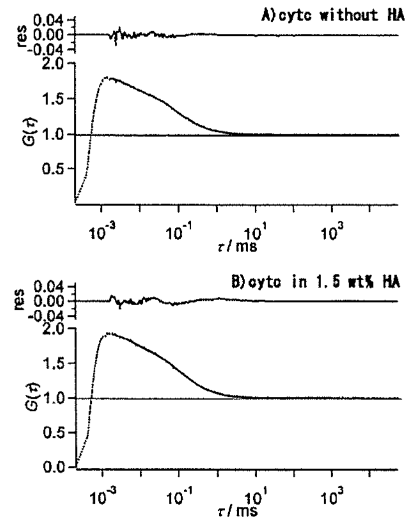

FIG. 2. Raw data of FCS correlation function $G(\tau)$ (in lower part of each figure) for cytc without (A) and with (B) HA plotted against correlation time τ on logarithmic scale. Solid lines express a fitting result to $G(\tau)$ with the function in Eq. (2). Each upper inset of raw data is the residue (res) after the fitting.

without large deviation from the theoretical function as seen in the residual functions. The absolute values of D_0 are indicated in Table I. For cytc, the absolute values and the HA concentration dependence of D_{obs} measured by FCS were similar to those found by PFG-NMR in our previous work.[30] For reference, previous results for cytc are shown in Fig. 1(b), namely, curve c together with curves $d-f$ corresponding to three other types of probe molecule. Curves $c-f$ are aligned in the order of their molecular size.

With the existence of HA in concentration C_{HA}, observed D_{obs} was reduced following a simple exponential law proposed by Ogston, Preston, and Wells[32] as

$$D/D_0=\exp(-aC_{\mathrm{HA}}^{0.5}), \tag{4}$$

where a is a constant that is related to ξ (the size of the mesh) and b (the effective diameter of probe molecule assuming a spherical molecular shape). If we use a simple scaling law assuming a cubic mesh of HA, we obtain

$$\xi=(b/a)C_{\mathrm{HA}}^{-0.5}. \tag{5}$$

We roughly estimated the b of each molecule from the structure, as shown in Table I, and ξ was estimated from the FCS and PFG-NMR curves in Fig. 1 to be 5 nm and 8 nm, respectively, for the solution of 1.5 wt% HA. The slight difference in fitting parameter a can be distinguished from the deviation between curves a and c. This difference will be discussed in Sec. III D after all the results from three kinds of methods are presented. Besides this small disagreement, the order of the mesh size agreed well with those of previous experimental results obtained by other methods,[26,27] indicating that all the solute molecules in FCS and PFG-NMR measurements are hindered by the network structure of HA. The overall result in Fig. 4 consistently indicates that the probe molecules are also retarded in the present FCS study.

TABLE I. Summary of observation time and diffusion distance observed for various molecules by three independent techniques PCBR (Ref. 30), PFG-NMR (Ref. 30), and FCS. τ_{obs} and L were calculated from the results in the absence of HA.

Diffusing probe molecules	Estimated molecular diameter b (nm)	Method	Nonperturbed diffusion coefficient D_0 ($\times 10^{10}$ m^2 s^{-1})	Observation time τ_{obs}	Diffusion distance L
cytc	3.4	PFG-NMR[a]	1.4	10–100 ms	3–9 μm
		FCS	1.4	67 μs	237 nm
		PCBR[a]	1.3	300–400 ns	15–18 nm
$[\mathrm{Ru}(bpy)_3]^{2+}$	1.0	PFG-NMR[a]	4.61	10–400 ms	5.3–33 μm
		PCBR[a]	4.6	300–400 ns	29–33 nm
Alexa	1.4	FCS	2.4	42 μs	246 nm
MV^{2+}	0.50	PFG-NMR[a]	7.93	30–70 ms	12–18 μm
		PCBR[a]	7.9	300–400 ns	38–44 nm
$\mathrm{Co}(acac)_3$	1.2	PFG-NMR[a]	4.86	100 ms	17 μm
$\mathrm{Co}(edta)^-$	0.8	PFG-NMR[a]	6.95	80 ms	18 μm
H_2O	0.30	PFG-NMR[a]	2.34	10–500 ms	3.7–26 μm

[a]Reference 30.

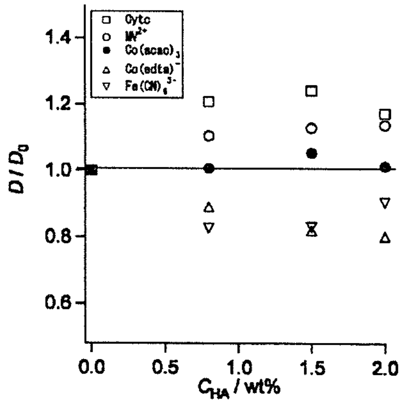

FIG. 3. Relative dependence of D_{obs} on C_{HA} using various quenchers observed by PCBR method. Slight dependence of D_{obs} on C_{HA} is apparently observed for charged molecules while almost no dependence was observed for a neutral quencher, Co$(acac)_3$. Since the ionic strength was induced by the existence of HA polymers, no intrinsic dependence on C_{HA} is expected for the charged molecules (see text).

B. Reinvestigation and correction of HA concentration dependence of diffusion coefficients in PCBR measurement

In our most recent paper,[30] we presented the results of D_{obs} obtained by the PCBR method with Ru$(bpy)_3^{2+}$ as a photosensitizer and cytc as a quencher. We estimated D_{obs} from the second-order rate constant of diffusion controlled quenching reactions. The lifetime of the excited states, which is about 300–400 ns, corresponds to the observation time of this method. However, a slight increase in D_{obs} from D_0 with C_{HA} was observed [Fig. 2(b) in Ref. 30]. To clarify this behavior, we performed further investigation of PCBR with other reaction systems. This time, we used a common photosensitizer Ru$(bpy)_3^{2+}$ as in our last study in combination with a variety of quenchers, i.e., cytc, MV^{2+}, Co$(acac)_3$, Co$(edta)^-$, and Fe(CN)_6^{3-}. In PCBR, the sum of Ds of Ru$(bpy)_3^{2+}$ and the employed quencher was obtained from the second-order rate constant of the intermolecular quenching reaction, then the individual D_{obs} of solutes must be prorated according to each molecular radius (see Ref. 30). D_0 values for new quenchers were also measured by PFG-NMR as indicated in Table I.

In Fig. 3, the C_{HA} dependence of the relative magnitudes of D_{obs} normalized to D_0 (D_{obs}/D_0) is shown. D_{obs} was almost independent of C_{HA} in the case of Co$(acac)_3$, while a slight C_{HA} dependence was observed for four other quenchers that possess positive or negative charges. (The total surface charge of cytc is $+9$.) This dependence is qualitatively explained by the influence of the additional ionic strength produced by HA polyanionic chains since the shielding effects induced by the ionic atmosphere accelerates the reaction between molecules that have charges with the same sign (homocharges) and decelerates that between molecules with heterocharges.[33,34] Thus the additional ionic atmosphere by the HA chains causes an overestimation of D_{obs} by PCBR for the combination of a positive quencher and a positive photosensitizer. The case reported in our previous paper was under the same conditions showing a slight increase of D_{obs} on HA addition.[30] Although it is possible[35] to convert the obtained result in an intrinsic self-diffusion constant by a quantitative correction with Debye-Smoluchowski theory, a detailed description of the ionic atmosphere produced by HA chains is still impossible because the effective ionic strength is not equal to that calculated from the prepared concentration of saccharide units which are linearly connected and not randomly distributed in the entire solution space. Here we simply concluded that D_{obs} for four charged particles is also independent of C_{HA} focusing the result for neutral Co$(acac)_3$. We use the D_0 values of cytc as the real values of D_{obs} in describing the DDDC plot shown in the following section.

C. Plot of the distance dependence of diffusion coefficient (DDDC)

In this study, we summarize the D_{obs} of cytc in HA solution obtained from FCS, PFG-NMR, and PCBR plot against the diffusion distance L (DDDC plot). A common probe molecule (cytc) was successfully used in three independent methods at various sampling times τ_{obs} in a wide range of 10^{-7}–10^{-1} sec (six orders). Since the obtained D_0 values of cytc for the three methods are mutually compatible as shown in Table I, we suppose that the three sets of data can be compared using their absolute values.

Although we simply refer to "diffusion distance" here, precise consideration is indispensable for describing DDDC with L. As long as we do not perform single-molecule spectroscopy, the distance L cannot be directly obtained from the real movement of each particle and can be evaluated only from the mean square displacement $\langle r^2 \rangle$ resulting from the ensemble average of a number of transporting molecules. In this study, we identify these two quantities, i.e., $L = \sqrt{\langle r^2 \rangle}$.

In homogeneous solutions where all interactions have neither time nor space correlation, the mean square displacement, $\langle r^2 \rangle$ increases linearly with time (normal diffusion).[3] Therefore, with the Fick's second law, L can be expressed with the diffusion coefficient D as a function of the diffusion time t for three-dimensional diffusion:

$$L = \sqrt{6Dt}. \tag{6}$$

D can be regarded as a connecting parameter between time t and space L as shown in Eq. (6). In widely used definition, D is defined as a parameter proportional to the differential coefficient of $\langle r \rangle^2$ with respect to time as

$$\frac{d}{dt}\langle r^2 \rangle = 2dD, \tag{7}$$

where d is the space dimensionality: $d=3$ for three-dimensional diffusion.

As is known from our previous studies,[30] the absolute value of D is still observable as D_{obs} even in *inhomogeneous* systems using the present three methods independently. We denote this experimental value as D_{obs}, stressing that it is no longer a universal constant (so-called diffusion constant) and depends on the sampling scale of time (or space) of each methodology.

Although the present three methods have different d values in each observation method, D can be obtained postulating that the diffusion is isotropic. Similarly, the D_{obs} obtained by each method is already an isotropic value with $d = 3$. Therefore, we borrow the form of Eq. (6) to express L with each observation period τ_{obs} and obtained D_{obs} using

$$L = \sqrt{6 D_{\mathrm{obs}} \tau_{\mathrm{obs}}}. \tag{8}$$

We can mutually change the time and space correlations using Eq. (8) and both values of L and τ_D are summarized in Table I including ones for other smaller molecules. The time and space correlations seem inseparable properties as two aspects of one phenomenon which can be mutually changed by Eq. (8) at any time. Once D_{obs} is determined by one experiment, the sampling gate function of which is known (in the cases of PCBR and PFG-NMR), we can obtain the counterpart space component, for example, as the mean square displacement $\langle r^2 \rangle$. Reversely, when D_{obs} is estimated by a method with an experimentally defined sampling space (in the case of FCS), we know the time correlation as an autocorrelation function in the process that determines D_{obs} by Eqs. (1)–(3). This autocorrelation function can be related to τ_D, the mean period of stay inside the confocal volume. In the present study treating the structural property of HA solution, however, the space parameter L is significant as a scaling marker to relate the variation of D_{obs} with the HA mesh size.

The actual values of τ_{obs} are determined from each set of experimental conditions using the following techniques. In PCBR, we used the lifetime of the excited state after quenching, which is a population average of the single exponential decay. (This is precisely correct as long as we assume homogeneous and isotropic quenching.) Since the phosphorescence lifetime of $\mathrm{Ru}(bpy)^{2+}$ is ≈ 300 ns, the observed diffusion was gated by this time constant and L of cytc was estimated to be ≈ 16–21 nm in PCBR.[30] In PFG-NMR, we regarded the duration period between two field gradient pulses as τ_{obs}. Since the duration time covers a wide area (10–100 ms), the estimated L of cytc was 2–9 μm.[30] Unlike the other two cases, L in FCS was directly defined from the optical setups of the applied apparatus using the horizontal scale parameter[36] w which is related to the translational diffusion time τ_D by Eq. (3). If we simply identify τ_D in Eq. (3) as τ_{obs}, L can be expressed as

$$L = \sqrt{6 D_{\mathrm{obs}} \tau_{\mathrm{obs}}} = \sqrt{6 D_{\mathrm{obs}} \tau_D} = \sqrt{3/2}\, w \tag{9}$$

in reference to Eq. (8).

Based on the consideration described above, we plotted the D_{obs} of cytc in 1.5 wt % HA solution against the logarithmic scale of L of each experiment, as shown in Fig. 4. At the lower limit of L, D_{obs} is expected to converge to D_0 because the effect of HA should be negligible without collision with polymer chains. The D_{obs} from PCBR is almost the same value as D_0 as described in Sec. III B. In two other points for FCS and PFG-NMR, the D_{obs} values were $\approx 30\%$ smaller than D_0 and exhibited a HA concentration dependence as fitted with Eq. (4). The DDDC line should become a step function connecting these four points. This plot can be discussed in conjunction with the behavior of the time correlation functions in dynamic light scattering (DLS)[37] experiments if they are plotted against τ_{obs} for gel solutions,[38] and colloidal suspension[14,39,40] whereby D_{obs} can be obtained as a function of τ_{obs}. Both D_{obs} plots against L and τ_{obs} are essentially the same in the presence of Eq. (8). In the present DDDC plot, L is chosen as the reference parameter stressing the space correlation of D_{obs} because this effect is caused by the spatial hindrance promoted by the network structure of HA polymer. The present DDDC covers more than three orders of L which correlates with six orders of τ_{obs} (see Table I).

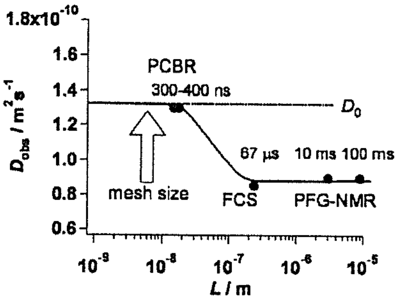

FIG. 4. A plot of distance dependence of diffusion coefficients (DDDC) plot of D_{obs} at $C_{\mathrm{HA}} = 1.5$ wt % against the averaged diffusion distance L on logarithmic scale. Since the D_{obs} obtained from PCBR experiment is increased by 28% by the ionic strength of the HA chain, D_0 was used as the intrinsic value assuming that D_{obs} without the effect of ionic atmosphere is almost equal to D_0 (see text). Furthermore, the curve should be extrapolated to D_0 at $L = 0$. The profile should be a step function with a sudden drop at 10–100 nm. The numbers indicated beside each point are τ_{obs} values corresponding to each experiment.

In Fig. 4, it is clearly shown that a jump of D_{obs} exists between the PCBR and the FCS points where L is ≈ 10–100 nm. This behavior should be related to some structural conditions of the HA solution in this scale region, as will be discussed in the following section.

D. HA network structure as observed by molecular diffusion

The order of the scale of the D_{obs} jump is consistent with the ξ from our present experiment (5 nm or 8 nm; marked in Fig. 4) because the mesh effect on diffusion coefficients is expected to appear in the same or 1–2 order larger scale than that of the mesh size.

As depicted in Fig. 4 showing a step function, the diffusion phenomena in aqueous HA solution are separated into two extreme modes which correlate with diffusion time and mesh size. (See Fig. 5.) When $L \ll \xi$ (short-diffusion mode), which is the case of PCBR, most of the trails of diffusing molecules are restricted in a space (pore) inside the mesh and the majority of the probe molecules have almost no opportunity to interact with the HA polymer chain. Eventually, D_{obs} approaches D_0 since it is the obtained statistical average of many molecules. On the other hand for $L \gg \xi$ (long diffusion mode), most of the probe molecules interact with networks many times, and the diffusion phenomena become similar to those found in continuous media with friction reducing D_{obs}. How much D_{obs} decreases is governed by the dynamics of the microscopic interaction between solutes and the HA chain. In Fig. 4, the short-diffusion area has $L < 10$ nm where D_{obs} takes a constant value of D_0. Since the D_{obs} value from FCS is approximately identical to that from PFG-NMR, D_{obs}

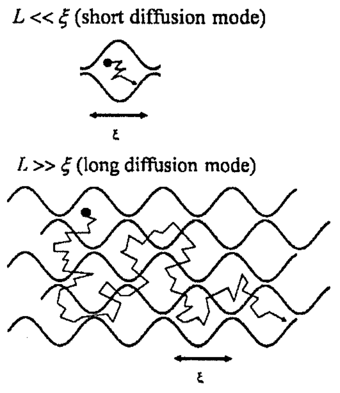

FIG. 5. Model of hyaluronan (HA) network structure which involves diffusive probe cytochrome c (cytc). The lower part of the figure shows the long-diffusion mode that was observed by FCS and PFG-NMR. The upper part of the figure shows the short-diffusion mode that is the case for PCBR.

in the long-diffusion area ($L > 100$ nm) is also likely to be a constant. In either of the long- or short-diffusion modes observed in the present system, the linear dependence of $\langle r^2 \rangle$ on time evolution is sustained and the diffusion process can be described as normal diffusion.

In the inhomogeneous systems, the effect of anomalous subdiffusion has been frequently mentioned[3,4] as one typical case of anomalous diffusion. The anomalous subdiffusion is generally accounted for by the phenomenon that the time derivative of $\langle r^2 \rangle$ for diffusing particles, which is a constant in normal diffusion, decreases in a longer time as, for example, $\langle r^2 \rangle \propto t^\alpha$ with $0 < \alpha < 1 : D_{\text{obs}}$ decrease with sampling period, i.e., $D_{\text{obs}} \propto \langle r^2 \rangle / t \propto t^{\alpha - 1}$ showing the time correlation. In FCS measurement, anomalous subdiffusion has been known to appear as a distortion of the autocorrelation function. The distorted function can be analyzed by a modified version of Eq. (2) obtained by replacing τ / τ_D with $(\tau / \tau_D)^\alpha$. For the present FCS point in Fig. 4, however, no distortion was observed in the correlation function that was in good agreement with the approximated function of Eq. (2) as shown in Fig. 2.

Since both the long and short diffusions showed no apparent anomalous characteristics, we suppose that the anomalous diffusion area lies in the transient area between two modes, which is unfortunately out of observable range in the present three methodologies. If we use a smaller molecule with a larger diffusion coefficient in combination with a larger mesh of more diluted HA solutions, this transient area should shift to a longer position of L and may be observable. We confirmed this in the experiment using smaller dye molecules (Rhodamine 123 and Alexa 488) dissolved in 0.1 wt % HA solution, the details of which will appear in a separate paper.

The DDDC curve should also include information about the distribution of ξ, that is, the uniformity of the mesh. The present results show a quick transition from short diffusion to long diffusion within a very narrow region ($L = 10-100$ nm). This implies that the distribution of the mesh size of HA is also in a narrow region. Therefore, the mesh size is quite uniform as long as we measure it through molecular diffusion. There are two possibilities for the mechanism giving a uniform mesh size: (a) The mesh size is statically uniform and (b) The mesh size is dynamically averaged by chain reorganization. We suppose that the second mechanism is more probable for the following reason. The long linear chains of high-molecular-weight HA are supposed to entangle by the hydrophobic interaction between the specific positions of saccharide units. Because of this weak interaction, the chains can constantly undergo reorganization, the time constant of which is unknown. In the present case of cytc, for example, the point giving the shortest τ_{obs} of the long-diffusion region ($L = 200$ nm, the point of FCS) corresponds to 67 μs. If we assume that the retardation effect of polymers is already averaged by chain motions in this range of τ_{obs}, the reorganization of a polymer chain may be faster or on a similar time scale. The diffusion coefficient of the HA chain in translational motion, D_{HA}, determined by FRAP was reported as $\sim 4.5 \times 10^{-12}$ m^2 s^{-1} for 500 kDa HA.[41] In spite of the difference in the molecular weight of the present HA (300 kDa), D_{HA} in this study is also expected to have a similar magnitude. Similarly, the local movement of HA chain may have the same order of amplitudes or lower. Therefore, this HA chain appears to move ≈ 43 nm within a τ_{obs} of ~ 67 μs for FCS observation, the length of which is one order larger than the mesh size of 1.5 wt % HA solution (5–8 nm).

As long as we use molecular diffusion to probe the mesh structure and its size, τ_{obs} for a certain L is always restricted by molecular size. That is, τ_{obs} and L are connected by the one-to-one relation of Eq. (8) as shown in Fig. 4. We have no other means of using various probing molecules with different radii over several orders to determine the time constant of HA chain movement in comparison with the particular τ_{obs} of each molecule. This method is almost impossible to apply in a practical use.

On the other hand, it should be noted that the effective ξ of 1.5 wt % HA solution obtained from the exponential fitting with Eqs. (4) and (5) for FCS (5 nm) was approximately 30% smaller than that for PFG-NMR (8 nm). We also attribute this small deviation to the contribution of some static structures which are partly observable in FCS but not in PFG-NMR due to dynamic averaging. In the present case, the average effect induced by chain reorganization should increase the effective mesh size, which implies that the removal of the hindrance opens a new pathway to probe molecules. As the result of dynamic chain motion, the volume of space reachable within the diffusion time increases providing a larger value of D_{obs} than that before the averaging. This deviation was prominent at low concentration showing that the FCS observation of a large mesh facilitates the detection of the static structure before the averaging. However, no apparent deviation from the theoretical curve of Eq. (2) was observed for these data points. Still around these points, the influence of inhomogeniety does not seem sufficiently strong to deform the theoretical curve of FCS but results in a small variation of the fitting parameter D_{obs}.

Finally, we would like to point out another valuable information about the HA matrix revealed from the DDDC plot in Fig. 4. The position of the transient area at 10-100 nm is at the border between the approximate sizes of nonliving materials (typically <10 nm) and some biological particles (cells, viruses, etc., typically >100 nm). This should be evidence of the important role of HA in ECM that controls the transport of particles according to their size such as in molecular sedimentation. One example is a cell in contact with ECM containing HA which can be described as follows. The C_{HA} dependence in Eqs. (4) and (5) should generate the concentration gradation of materials secreted from a point in the plasma membrane or its entire surface. This gradation function is modulated by the existence of HA and precious materials are not likely to diffuse away from the surface area of the cell. The HA matrix in ECM holds moisture similarly to a cotton ball of "nanostrings" (which is called nanocotton) covering the cell surface with aqueous solutions. At the same time, a thin solution area of 10–100 nm thickness is formed around the cell surfaces where various molecules are held, diffuse as smoothly as ordinary aqueous solutions reaching some reaction points easily, and change their orientations quickly to interact or react with some substances on the plasma membrane.

Apparently, one significant role of ECM containing HA and other materials such as collagens should be in the control of material transports, probably through the time and space correlations of mass transports which include so-called anomalous diffusion. A large part of the wide variety of ECM functions such as those in cell adhesion, tumor cell migration, nourishing organisms, and developments can be explained on the basis of anomalous diffusion in inhomogeneous media. This approach using the DDDC plot will also benefit the development of ECMs and artificial ECMs for medical applications such as the control of drug delivery and the arrest of cancer.[7]

CONCLUSION

In conclusion, we obtained a DDDC plot for cytc dissolved in aqueous HA solution. It showed a considerable space correlation of the observable diffusion coefficient. This characteristic behavior of HA can be related to its function in ECM of controlling material transport to realize a suitable environment for various bioactivities.

ACKNOWLEDGMENTS

The authors are grateful to Dr. Teruzo Miyoshi of Denki-Kagaku Kogyo K. K. and Mr. Yasufumi Takahashi of Chugai Pharmaceutical Co., Ltd. for their assistance in the HA study. This project was partly supported by the Presidential Research Grant for Intersystem Collaboration of Riken and The Cosmetology Research Foundation.

[1] J.-P. Bouchaud and A. Georges, Phys. Rep. **195**, 127 (1990).
[2] S. Havlin and D. Ben-Avraham, Adv. Phys. **36**, 695 (1987).
[3] P. A. Netz and T. Dorfmüller, J. Chem. Phys. **107**, 9221 (1997).
[4] M. J. Saxton, Biophys. J. **56**, 615 (1989); **66**, 394 (1994).
[5] Y. Gefen, A. Aharony, and S. Alexander, Phys. Rev. Lett. **50**, 77 (1983).
[6] J.-P. Bouchaud and A. Georges, in *Disorder and Mixing: Convection, Diffusion and Reaction in Random Materials and Processes,* edited by E. Guyon, J. P. Nadal, and Y. Pomeau (Kluwer Academic, Dordrecht, 1988), pp. 19-29.
[7] G. Alexandrakis, E. B. Brown, R. T. Tong, T. D. McKee, R. B. Campbell, Y. Boucher, and R. K. Jain, Nat. Med. **10**, 203 (2004).
[8] M. Weiss, H. Hashimoto, and T. Nilsson, Biophys. J. **84**, 4043 (2003).
[9] T. V. Ratto and M. L. Longo, Langmuir **19**, 1788 (2003).
[10] J. R. Lead, K. Starchev, and K. J. Wilkinson, Environ. Sci. Technol. **37**, 482 (2003).
[11] K. Starchev, J. Sturm, G. Weill, and C.-H. Brogren, J. Phys. Chem. B **101**, 5659 (1997).
[12] T. Narita, A. Knaebel, J.-P. Munch, and S. J. Candau, Macromolecules **34**, 8224 (2001).
[13] R Klein, in *Structure and Dynamics of Polymer and Colloid Systems*, edited by R. Borsali and R. Pecora (Kluwer Academic, Dordrecht, 2002), pp. 83–115.
[14] P. N. Pusey and R. J. A. Tough, in *Dynamic Light Scattering: Applications of Photon Correlation Spectroscopy*, edited by R. Pecora (Plenum, New York, 1985), pp. 85–175.
[15] X. Cao and M. S. Shoichet, Neuroscience **103**, 831 (2001).
[16] N. McDowell, A. M. Zorn, D. J. Crease, and J. B. Gurdon, Curr. Biol. **7**, 671 (1997).
[17] J. B. Gurdon, P. Harger, A. Mitchell, and P. Lemaire, Nature (London) **371**, 487 (1994).
[18] M. T-Lavigne and M. Placzek, Trends Neurosci. **14**, 303 (1991).
[19] T. C. Laurent, B. N. Preston, B. Gustafsson, and M. McCabe, Eur. J. Biochem. **53**, 129 (1975).
[20] B. N. Preston, B. Öbrink, and T. C. Laurent, Eur. J. Biochem. **33**, 401 (1973).
[21] J. E. Scott, in *The Biology of Hyaluronan*, edited by D. Evered and J. Whelan (Wiley, Chichester, UK, 1989), pp. 6–20.
[22] J. E. Scott, in *Chemistry, Biology and Medical Applications of Hyaluronan and Its Derivatives*, edited by T. C. Laurent and E. A. Balazs (Portland, London, 1998), pp. 7–16.
[23] J. E. Scott, in *New Frontiers in Medical Sciences: Redefining Hyaluronan*, edited by G. Abatangelo and P. H. Weigel (Elsevier Science, Amsterdam, The Netherlands, 2000), pp. 11–19.
[24] L. Lapčík, Jr., L. Lapčík, S. De Smedt, J. Demeester, and P. Chabreek, Chem. Rev. **98**, 2663 (1998).
[25] B. Alberts, A. Johnson, J. Lewis, M. Raff, K. Roberts, and P. Walter, *Molecular Biology of the Cell*, 4th ed. (Garland Science, New York, 2001), pp. 1092–1112.
[26] S. C. De Smedt, A. Lauwers, J. Demeester, Y. Engelborghs, G. De Mey, and M. Du, Macromolecules **27**, 141 (1994).
[27] V. Shenoy, J. Rosenblatt, J. Vincent, and A. Gaigalas, Macromolecules **28**, 525 (1995).
[28] T. Kluge, A. Masuda, K. Yamashita, and K. Ushida, Macromolecules **33**, 375 (2000).
[29] T. Kluge, A. Masuda, K. Yamashita, and K. Ushida, Photochem. Photobiol. **68**, 771 (1998).
[30] A. Masuda, K. Ushida, H. Koshino, K. Yamashita, and T. Kluge, J. Am. Chem. Soc. **123**, 11468 (2001).
[31] *Fluorescence Correlation Spectroscopy: Theory and Applications*, Springer Series in Chemical Physics, Vol. 65, edited by R. Rigler and E. S. Elson (Springer, Berlin, 2001).
[32] A. G. Ogston, B. N. Preston, and J. D. Wells, Proc. R. Soc. London, Ser. A **333**, 297 (1973).
[33] S. R. Logan, Trans. Faraday Soc. **62**, 3416 (1966).
[34] J. I. Steinfeld, J. S. Francisco, and W. L. Hase, *Chemical Kinetics and Dynamics*, 2nd ed. (Prentice Hall, Upper Saddle River, NJ, 1999) p. 124.
[35] C. Chiorboli, M. T. Indelli, M. A. R. Scandola, and F. Scandola, J. Phys. Chem. **92**, 156 (1988).
[36] E. L. Elson and D. Magde, Biopolymers **13**, 1 (1974).
[37] B. J. Berne and R. Pecora, *Dynamic Light Scattering with Applications to Chemistry, Biology, and Physics* (Dover, New York, 2000).
[38] Y. Suzuki and I. Nishio, Phys. Rev. B **45**, 4614 (1992).
[39] P. N. Pusey, J. Phys. A **11**, 119 (1978).
[40] P. N. Pusey, Philos. Trans. R. Soc. London **A293**, 429 (1979).
[41] P. Gribbon, B. C. Heng, and T. E. Hardingham, Biophys. J. **77**, 2210 (1999).

A EUROPEAN JOURNAL

CHEM CHEM

OF CHEMICAL BIOLOGY

Table of Contents

Y. Nomura, M. Kinjo*

1701 – 1703

Real-Time Monitoring of in vitro Transcriptional RNA by Using Fluorescence Correlation Spectroscopy

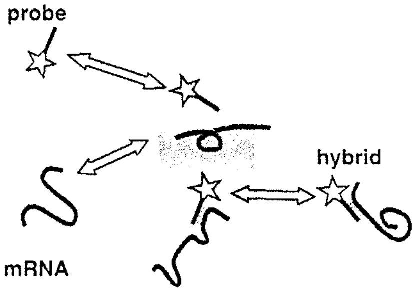

The autocorrelation function of a fluorescent probe has been analyzed by the two-component model with a free probe and a bound form of the hybrid (see figure). The fraction of the slow component increased with the reaction time; this corresponds to the increase in transcripts. In vitro transcriptional RNA can be detected in a sequence-specific manner without any denaturants.

WILEY-VCH

Real-Time Monitoring of in vitro Transcriptional RNA by Using Fluorescence Correlation Spectroscopy

Yasutomo Nomura*[a, b] and Masataka Kinjo[c]

In vitro transcription is widely used to synthesize small amounts of RNA from recombinant DNA templates.[1] In the conventional analysis of transcripts, northern blotting is used as a technique for size fractioning the RNA in a denaturing gel. In this study, we provide a novel technique to monitor in vitro transcriptional RNA synthesis without any denaturants while the reaction is progressing. Fluorescence correlation spectroscopy (FCS) sensitively measures fluctuations in fluorescence intensity, due to only a few fluorescent molecules that diffuse in and out of a small volume element at the subfemtoliter level in solution, which are dependent on the molecular weight and the concentration.[2–5] Recently, this method was applied to measuring diffusion and the hybridization state of oligo(dT) and poly A in mRNA within living cells.[6] However, it is difficult to detect a specific mRNA by using oligo(dT).

In the present study, two plasmids encoding the luciferase gene and *Xenopus* elongation factor-1α were used as templates for transcription. We determined the interaction between these transcripts and labeled 23-mer oligo-DNAs (GL primer), complementary to the sequence of the luciferase RNA or 30-mer oligo(dA). The fluorescence correlation functions were analyzed by using a simple two-component model with a fast-moving component of free GL primer and a slow-moving component of the hybrid.

The secondary structure of the luciferase RNA (site 1–1700) was simulated. In the predicted structure, three sites (52–54, 57–62, and 68–74) in the 52–74 sequence, complementary to the GL primer, interacted with different sites of the same molecule by base-pairing. This suggests the difficulty of binding between the GL primer and the luciferase RNA after folding to form a secondary structure.

The plasmid-encoding luciferase gene (*pLuc*, site 1–1700) was linearized by *Eco*RV (*pLuc*/*Eco*RV). The site 1–1389 was transcribed from *pLuc*/*Eco*RV. Figure 1 shows typical autocorrelation functions of the fluorescent oligo-DNAs in the reaction solution at the various times after the addition of *pLuc*/*Eco*RV as a template. The normalized autocorrelation function of the GL primer was shifted to the right with a reaction time of 120 min; this suggests that there is an interaction between the probe and the larger molecules. In the case of oligo(dA), the autocorrelation function was not shifted (see insert). The results indicated that the GL primer hybridized with the luciferase transcripts before they folded to form a secondary structure. Furthermore, there was no significant difference between the diffusion time of the GL primer and oligo(dA) in the in vitro transcription system with pXef-1, which is a linearized plasmid DNA that contains the *Xenopus* elongation factor-1α gene (see Table 1). Neither fluorescent oligo-DNA probe was complementary to the pXef-1 transcript. Thus, these results indicated that the GL primer hybridized with transcripts of *pLuc*/*Eco*RV in a sequence-specific manner.

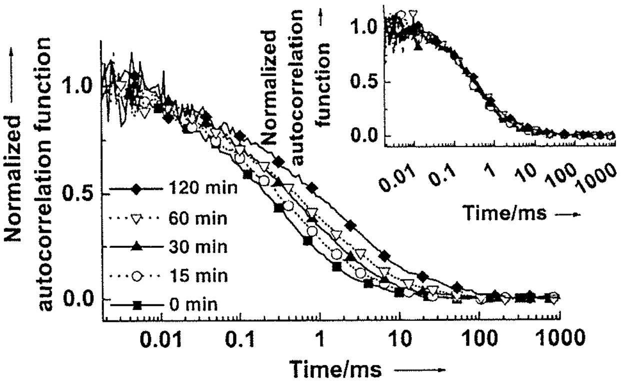

Figure 1. Normalized autocorrelation functions of in vitro transcription products of pLuc/EcoRV*. Fluorescence fluctuation was probed with a GL primer and with oligo(dA) (insert). Different curves show autocorrelation functions at various reaction times after the addition of the plasmid. Both symbols and lines represent experimental data. The concentration of* pLuc/EcoRV *was 0.1 μg.*

Although the autocorrelation function of the GL primer just after the addition of *pLuc*/*Eco*RV could be fitted well by using the one-component model, it was difficult to analyze data from 15 to 120 min. In every transcription reaction, the translational diffusion time of the free fast-moving probe was estimated from the autocorrelation function at 0 min, and the mean time was 0.39 ms ($n=4$) in Table 1. Using this diffusion time of the fast component as a constant value, we analyzed data from 15 to 120 min with the two-component model, and the autocorrelation function could be fitted well. As shown in Figure 2, the fraction of the slow component increased greatly from 0.20 at 15 min to 0.55 at 120 min; this agreed with the relative band intensity from the densitometric analysis after gel electrophoresis. In contrast, the diffusion time was relatively stable, although there was a slight increase from 3.4 to 5.7 ms. The reason for the slight increase is unclear, nevertheless we observed bands near base 1400 at every reaction time in the gel electrophoresis. These data suggested that, using FCS, we detected the increase in number of the slow component rather than that in the length during in vitro transcriptional RNA synthesis.

---

[a] Dr. Y. Nomura
Department of Bio-System Engineering, Faculty of Engineering
Yamagata University, Yonezawa 992-8510 (Japan)
Fax: (+81) 238-26-3357
E-mail: ynomura@yz.yamagata-u.ac.jp

[b] Dr. Y. Nomura
Current address:
Department of Environmental Life Science
Graduate School of Medical Science
Yamagata University, Yonezawa, Yamagata 992-8510 (Japan)
Fax: (+81) 238-26-3357

[c] Dr. M. Kinjo
Laboratory of Supramolecular Biophysics
Research Institute for Electronic Science, Hokkaido University
Sapporo 060-0812 (Japan)

DOI: 10.1002/cbic.200400046

Table 1. Diffusion time (ms) of oligonucleotides in transcription system.[a]

Probe	plasmid	none	pXef-1	*pLuc/Eco*RV		*pLuc/Eco*RI	
GL primer	fitting	1 component	1 component	2 components		2 components	
				Fast	Slow	Fast	Slow
	Diffusion time	0.38	0.58[d]	0.39	5.71	0.35	1.66
		(0.05)	(0.15)	(0.03)	(0.17)	(0.05)	(0.32)
	Fraction	–	–	0.45	0.55	0.49	0.51
				(0.10)	(0.10)	(0.15)	(0.15)
	Sample[b]	7	2	4		3	
	Data points[c]	26	7	19		12	
Oligo (dA)	fitting	1 component	1 component	1 component		1 component	
	Diffusion time	0.33	0.61[e]	0.64[f]		0.63[f]	
		(0.04)	(0.27)	(0.14)		(0.09)	
	Sample	2	3	3		3	
	Data points	9	11	9		11	

[a] Each diffusion time is the mean (SD) at 120 min after the addition of plasmid. [b] The values were measured in the different numbers of samples shown in the table. [c] Three to five values were obtained from each sample. [d] Significantly different from values of GL primer in the absence of pXef-1, $P < 0.005$. [e] Significantly different from values of oligo A in the absence of pXef-1, $P < 0.01$. [f] Significantly different from values of oligo A in the absence of the plasmids, $P < 0.005$.

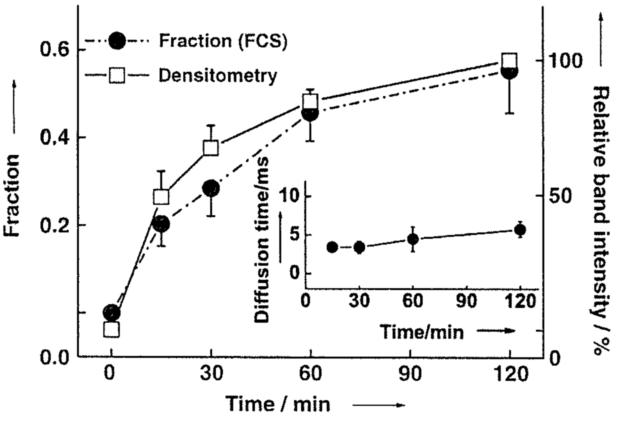

Figure 2. Fractions and diffusion times (insert) of the slow component in pLuc/Eco*RV transcripts at different reaction times (n = 4). A GL primer was used. Each autocorrelation function was fitted to the two-component model. The diffusion time of the fast component was fixed at 0.39 ms. The band intensities of transcripts from gel electrophoresis were also estimated.*

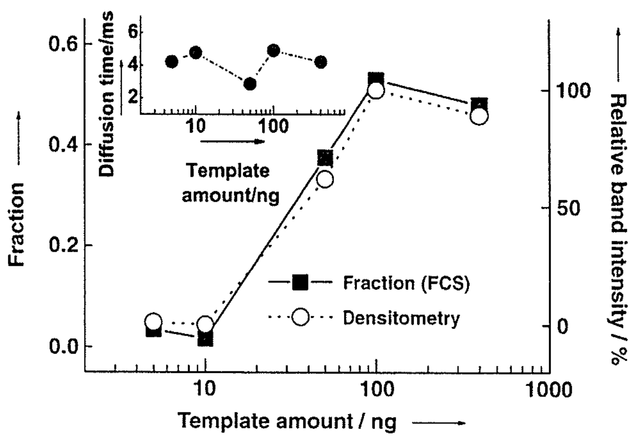

Figure 3. Dependency of template amount on fraction and diffusion time (insert) of the slow component in the transcription reaction with pLuc/Eco*RV at 120 min. A GL primer was used. The band intensities of transcripts from gel electrophoresis were also estimated.*

Next, *pLuc* was linearized by *Eco*RI (*pLuc/Eco*RI). The site 1-638 was transcribed from *pLuc/Eco*RI. Using the GL primer, we compared the diffusion times of transcripts of *pLuc/Eco*RV with those of *pLuc/Eco*RI (Table 1). The fraction of the slow component that had a diffusion time of 5.71 ms in the case of *pLuc/Eco*RV increased with reaction time and was 0.55 at 120 min. On the other hand, in *pLuc/Eco*RI, the fraction of the slow component increased to 0.51 at 120 min, but the diffusion time was 1.66 ms. Each transcript was also analyzed by gel electrophoresis after being quantified by FCS measurement. As expected, bands near bases 600, 1400, and 1900 were detected for transcripts with *pLuc/Eco*RI, *pLuc/Eco*RV, and pXef-1, respectively (data not shown). Therefore, FCS can measure diffusion time dependent on base length.

The autocorrelation functions of fluorescent probes in reaction solutions that contained from 5 to 400 ng plasmid DNA were analyzed by using the two-component model, as shown in Figure 3. FCS measurement was carried out at 120 min after the addition of plasmids. For the reaction from 5 to 10 ng of plasmid DNA, only a small fraction of the slow component was observed between 0.02 and 0.03. At 100 ng of *pLuc/Eco*RV plasmid DNA, the fraction increased to 0.53. The transcription reaction reached the plateau phase at 400 ng. According to the instruction manual of this transcription system, 20 µL reaction mixture containing 1 µg of templates that encode for 1.9 kb transcript synthesized 50 µg of RNA after 120 min of incubation. Although this suggests that the contents of our transcripts would be much more than that of the labeled primer, the reason for the observation of a large fraction of unbound probes is unclear. In contrast to the changes in this fraction, the diffusion time varied between 2.9 and 4.9 ms, but the upward tendency were not observed. These results agree with those from densitometric analysis of the gel.

Recently fluorescence resonance energy transfer (FRET) has been used to detect the specific mRNA in transcription systems in in vitro and in living cells.[7,8] Since FRET, unlike FCS, depends on the real distance between donor and acceptor, the sequences of the probes must be based on the 3D structure of RNA. Northern analysis is the only conventional method for size fractionating RNA, but this must be performed on the denatured gel. In contrast, FCS did not require any denaturants because the hybrid of the probe with the synthesized RNA before the formation of secondary structure was measured directly. Furthermore, since FCS measurement causes little damage, we can use the sample even after measuring for different experiments.

FCS permits real-time monitoring of specific RNA in an in vitro transcription system in which the fluorescent oligonucleotide probe was complementary to the coding sequence of RNA.

Experimental Section

The in vitro transcription reaction was carried out with a T7 MEGAscript (Ambion) kit system. The two expression plasmids used in this study were *pLuc* (Promega) and pXef-1(Ambion). Two fluorescent oligo-DNAs were purchased from Sigma Genosys. One was 5′-rhodamine green-CTTTATGTTTTTGGCGTCTTCCA-3′ (23-mer). The other was 5′-rhodamine green-oligo(dA)-3′ (30-mer).

The sequence of luciferase RNA used for the simulation was obtained from the Promega Corp. Simulation of the secondary structure of the luciferase RNA was performed by using Vienna RNA software.[9] FCS measurement was performed by using a ConfoCor fluorescence correlation measurement system (Carl Zeiss Jena GmbH, Jena, Germany) as described elsewhere.[10] The in vitro transcription solution was separated by electrophoresis on formaldehyde denaturing gel (agarose 1 %).

Acknowledgements

This study was supported in part by Grants-in-Aid for Scientific Research (C) (2) (14580761) from the Ministry of Education, Science, Sports and Culture of Japan.

Keywords: correlation · diffusion · fluorescence spectroscopy · hybridization · RNA

[1] R. Davis, *Curr. Opin. Biotechnol.* **1995**, *6*, 213–217.
[2] S. Maiti, U. Haupts, W. W. Webb, *Proc. Natl. Acad. Sci. USA* **1997**, *94*, 11 753–11 757.
[3] R. Pecora, S. Aragon, *J. Chem. Phys.* **1976**, *64*, 1791–1803.
[4] N. G. Walter, P. Schwille, M. Eigen, *Proc. Natl. Acad. Sci. USA* **1996**, *93*, 12 805–12 810.
[5] M. Kinjo, R. Rigler, *Nucleic Acids Res.* **1995**, *23*, 1795–1799.
[6] J. C. Politz, E. S. Browne, D. E. Wolf, T. Pederson, *Proc. Natl. Acad. Sci. USA* **1998**, *95*, 6043–6048.
[7] Y. Sei-Iida, H. Koshimoto, S. Kondo, A. Tsuji, *Nucleic Acids Res.* **2000**, *28*, E59.
[8] A. Tsuji, H. Koshimoto, Y. Sato, M. Hirano, Y. Sei-Iida, S. Kondo, K. Ishibashi, *Biophys. J.* **2000**, *78*, 3260–3274.
[9] I. L. Hofacker, *Nucleic Acids Res.* **2003**, *31*, 3429–3431.
[10] Y. Nomura, H. Tanaka, L. Poellinger, F. Higashino, M. Kinjo, *Cytometry* **2001**, *44*, 1–6.

Received: February 13, 2004

ARTICLE IN PRESS

ELSEVIER

Available online at www.sciencedirect.com

SCIENCE DIRECT®

Biochemical and Biophysical Research Communications 324 (2004) 1264–1273

BBRC

www.elsevier.com/locate/ybbrc

Molecular dynamics of STAT3 on IL-6 signaling pathway in living cells

Kenji Watanabe[a], Kenta Saito[b], Masataka Kinjo[b], Tadashi Matsuda[c], Mamoru Tamura[b], Shigeyuki Kon[a], Tadaaki Miyazaki[a,*], Toshimitsu Uede[a]

[a] *Division of Molecular Immunology, Institute for Genetic Medicine, Hokkaido University, N15 W7, Kita-ku, Sapporo 060-0815, Japan*
[b] *Laboratory of Supramolecular Biophysics, Research Institute for Electronic Science, Hokkaido University, N12 W6, Kita-ku, Sapporo 060-0812, Japan*
[c] *Department of Immunology, Graduate School of Pharmaceutical Sciences, Hokkaido University, N12 W6, Kita-ku, Sapporo 060-0812, Japan*

Received 24 September 2004

Abstract

Signal transducer and activator of transcription 3 (STAT3) is a critical signal transducer of interleukin-6 (IL-6) signaling. To investigate the mobility and the dynamics of STAT3 complex on IL-6 signaling in living cells, we generated a chimeric gene consisting of STAT3 fused to enhanced green fluorescence protein, STAT3-GFP. STAT3-GFP was expressed in Hep3B cells and the dynamics of this protein were analyzed by fluorescence correlation spectroscopy. After IL-6 stimulation, STAT3 translocated from the cytoplasm to the nucleus, as shown previously. According to the analysis of STAT3 diffusion in stable transformants, the number of STAT3 molecules at the cytoplasmic membrane and in the cytoplasm decreased after IL-6 stimulation. In the nucleus, the diffusion speed of STAT3 complex strongly decreased after IL-6 stimulation. Furthermore, we found that STAT3 existed as a complex whose molecular weight was less than 400 kDa before IL-6 addition. However, IL-6 stimulation induced the formation of STAT3 dimer as a megacomplex form whose molecular weight was more than 1 MDa at the cytoplasm and a very slow diffusion complex in the nucleus.

Keywords: Fluorescence correlation spectroscopy; Signal transducer and activator of transcription 3; Enhanced green fluorescence protein; Interleukin-6; Diffusion constant; Megacomplex form

Due to recent technological advances, it has become possible to measure the dynamics of single-molecule proteins in living cells. Fluorescence correlation spectroscopy (FCS) is one of the techniques to assess protein–protein interactions in aqueous solutions at the single molecule level [1]. In brief, the fluorescence intensity fluctuations caused by fluorescent probe movement are detected in a very small, well-defined open volume (0.25 fl). The diffusion constant and the absolute number of fluorescent molecules are deduced from the fluorescence autocorrelation function (FAF), calculated from the data of measured fluctuations. We estimate the change in the degree of molecular interaction by using the diffusion constant. Therefore, FCS has been applied to the analysis of molecular dynamics and interactions in solution [2–11].

Signal transducers and activators of transcription 3 (STAT3) is one of the STAT family of proteins which has been shown to play pivotal roles in the cytokine signaling pathway [12,13], and also in regulating cell growth and differentiation. STAT3 is activated by stimulation with interleukin-6 (IL-6) which is a multifunctional cytokine that regulates immune response, hematopoiesis, neural differentiation, and acute phase reaction [14–17]. The mechanism of the STAT3 signaling pathway has been investigated by biological

---

[*] Corresponding author. Fax: +81 11 706 7542.
E-mail address: miyazaki@igm.hokudai.ac.jp (T. Miyazaki).

0006-291X/$ - see front matter © 2004 Elsevier Inc. All rights reserved.
doi:10.1016/j.bbrc.2004.09.187

experiments [12–21]. IL-6 binds to the soluble or surface-attached IL-6 receptor α-chain (IL-6Rα) and this binary complex then binds to the signal transducer, gp130, inducing dimerization of gp130. This dimerization triggers activation of the Janus protein tyrosine kinase (JAK) 1 and JAK2 associated with the cytoplasmic tail of gp130. JAK activation is induced by tyrosine (Tyr) phosphorylation [12–14]. These phosphorylated Tyr residues in the cytoplasmic tail of gp130 are thought to recruit monomeric STAT3 via the src homology domain 2 (SH2) of STAT3. This recruitment is followed by Tyr phosphorylation of STAT3 by the JAKs, and phosphorylated STAT3 molecules dissociate from gp130 and generate STAT3 homodimers or STAT3–STAT1 heterodimers [20,22,23]. These STAT3 complexes translocate from the cytoplasm to the nucleus and only STAT3 homodimers bind to the target DNA motifs [20,21,23].

The functional role and activation mechanism of the STAT family of proteins have been well investigated. However, the molecular state of STAT molecules on cytokine signaling in living cells is still unknown. Recently, the statosome model has been proposed [24] in addition to the above-mentioned standard model [21]. In the standard model, it was predicted that STAT3 does not form a complex with other molecules. However, in the recent statosome model, it is predicted that STAT3 associates with other proteins and the sizes of these molecular complexes are in the range of 200–400 kDa (statosome I) and 1–2 MDa (statosome II). Indeed, it was reported that STAT3 associated with glucose regulated protein 58 (GRP58), caveolin-1 (cav1), and heat shock protein 90 (HSP90) [24–29].

In this study, we generated a fusion protein of STAT3 with green fluorescence protein (GFP) and traced the distribution of this fusion protein by laser scanning microscope (LSM). We were able to detect a change in the number of STAT3 molecules at the cytoplasmic membrane, in the cytoplasm, and in the nucleus before and after IL-6 stimulation. In addition, the diffusion speed of STAT3 complex was measured in these areas before and after IL-6 stimulation. Furthermore, the molecular size of the complex form of STAT3 fusion protein in living cells was determined by FCS. These analyses led to clarification of the change in number, diffusion speed, complex size, and molecular state of STAT3 proteins in a small area of the cell before and after IL-6 stimulation in a living cell.

Materials and methods

Reagents, cell culture, and transfection with plasmid DNA. Human recombinant IL-6 was a gift from Ajinomoto and plasmid for murine STAT3 cDNA was a gift from Dr. T. Hirano. The human hepatoma cell line, Hep3B, was cultured in a 5% CO_2 humidified atmosphere at 37 °C in Dulbecco's modified Eagle's medium (DMEM) supplemented with 10% fetal calf serum. Stable Hep3B cell line was generated by transfection of the expression vectors for mSTAT3 fused to EGFP-N1 (Clontech, Palo Alto, CA, USA) and selection by using G418 (600 μg/ml). For the transient expression of enhanced green fluorescence protein (EGFP), cells were plated at a confluence of 10–20% on LAB-TEK chambered coverslips with eight wells (Nalge Nunc International, Naperville, IL, USA) for 12 h before transfection. Five minutes after mixing of DMEM (50 μl) and FuGENE 6 (1.2 μl, Roche Molecular Biochemicals, Mannheim, Germany), 0.8 μg of the EGFP-N1 was added to this prediluted FuGENE 6 solution. The DNA solution was left for 15 min and added to each well at 30 h before FCS measurement.

Microscopy. Live cell fluorescence microscopy was performed using inverted confocal laser scanning microscope 510 (LSM, Carl Zeiss, Jena, Germany). EGFP molecule was excited at the 488 nm laser line of a CW Ar^+ laser through a water immersion objective (C-Apochromat, 40×, 1.2 NA; Carl Zeiss) with emission objective 505 nm. Pinhole diameter was adjusted to 70 μm.

FCS setup. FCS measurements were carried out by ConfoCor2 (Carl Zeiss) that consisted of a CW Ar^+ laser, a water immersion objective (C-Apochromat, 40×, 1.2 NA; Carl Zeiss), and an avalanche photodiode (SPCM-200-PQ, EG&G, Quebec, QC, Canada). Confocal pinhole diameter was adjusted to 70 μm. Samples were excited with about 10 kW/cm^2 of laser power at 488 nm and the fluorescence signal was detected through a dichroic mirror (>510 nm) and a band pass filter (515–560 nm).

FCS measurement and analysis. Cells were washed with phenol red free OPTI-MEM I (Gibco) two times to remove phenol red dye, and then the medium was replaced by OPTI-MEM I. After 6 h, FCS measurements were carried out. Activation of STAT3 was done by addition of IL-6 (50 ng/ml) to the culture medium. Obtained FAF were fitted by a one-, two-, or three-component model as follows:

$$G(\tau) = \frac{\langle I(t)I(t+\tau)\rangle}{\langle I(t)\rangle^2} = 1 + \frac{1}{N}\sum_i F_i\left(1+\frac{\tau}{\tau_i}\right)^{-1}\left(1+\frac{\tau}{s^2\tau_i}\right)^{-1/2}, \qquad (1)$$

where F_i and τ_i are the fraction and diffusion time of component i, respectively, N is the number of fluorescence molecules in the detection volume element defined by $s = z_0/w_0$, radius w_0 and length $2z_0$. The correlation amplitude of the function (y intercept, the value of $G(0)$) is determined by the reciprocal of the number of fluorescence molecules in detection volume. FAFs of rhodamine 6G (Rh6G) solution were measured for 30 s five times at 10 s interval, then the diffusion time (τ_{Rh6G}) and s were obtained by one-component fitting of the measured FAFs. Diffusion constants of samples (D_{sample}) were calculated from the ratio with the diffusion constant of Rh6G D_{Rh6G} ($2.8 \times 10^{-6}\ cm^2 s^{-1}$) and the diffusion times τ_{Rh6G} and τ_{sample} were obtained as the following equation:

$$\frac{D_{sample}}{D_{Rh6G}} = \frac{\tau_{Rh6G}}{\tau_{sample}}. \qquad (2)$$

Result

Time course analysis of STAT3 localization after IL-6 stimulation

Localization of STAT3-GFP and enhanced green fluorescence protein (EGFP) in Hep3B cells were independently measured by a confocal laser scanning microscope (LSM) before and after IL-6 addition. No change of the localization was observed for EGFP expressed in Hep3B cells by confocal images after IL-6 addition (Fig. 1, left panel). On the other hand, localization change of